Tomita and Kido *Earth, Planets and Space* (2022) 74:176
https://doi.org/10.1186/s40623-022-01740-0

Earth, Planets and Space

TECHNICAL REPORT

Open Access

An approximate travel time calculation and a robust GNSS-acoustic positioning method using an MCMC technique

Fumiaki Tomita* and Motoyuki Kido

Abstract

It is important to consider horizontal heterogeneity in an underwater sound speed structure to accurately estimate positions of GNSS-acoustic sites. Although large amounts of moving survey data (a sea-surface platform moves around when acoustic signals are transmitted) are required to accurately detect a sloping sound speed structure, the actual observational data do not necessarily include sufficient moving survey data due to sea conditions or observational time. To treat these insufficient data, it was assumed that a shallow sound speed gradient was continuously present up to a fixed water depth (gradient depth). However, the validity of this assumption has not been investigated, and the gradient depth has not been optimized. In this study, we developed a new GNSS-acoustic array positioning method that optimizes the gradient depth using an MCMC technique. To employ this technique, we also developed an approximate technique for rapidly calculating travel time, because the conventional travel time calculation requires high computational cost for integration into the MCMC technique. We assessed the performance of the approximate travel time calculation technique and demonstrated its sufficient accuracy and precision for estimating array positions. Then, we applied the new GNSS-acoustic array positioning method to the actual observational data collected by the Japan Coast Guard and Tohoku University. Using enough amounts of the moving survey data, our method demonstrated the results comparable with the conventional GNSS-acoustic positioning method estimating a sloping sound speed structure; thus, the assumption of the sound speed gradient with the fixed water depth was valid. Moreover, due to the physical restriction of this assumption, our method provided robust solutions even when the observational data contained small quantities of moving survey data with a simple sea-surface track. Although our method still cannot be used in the scenario, where no moving survey data are available, it can work robustly compared with the conventional methods.

Keywords: GNSS-A positioning, Seafloor geodesy, Travel time calculation, Markov chain Monte Carlo

*Correspondence: fumiaki.tomita.d8@tohoku.ac.jp

International Research Institute of Disaster Science, Tohoku University, Sendai, Japan

Graphical Abstract

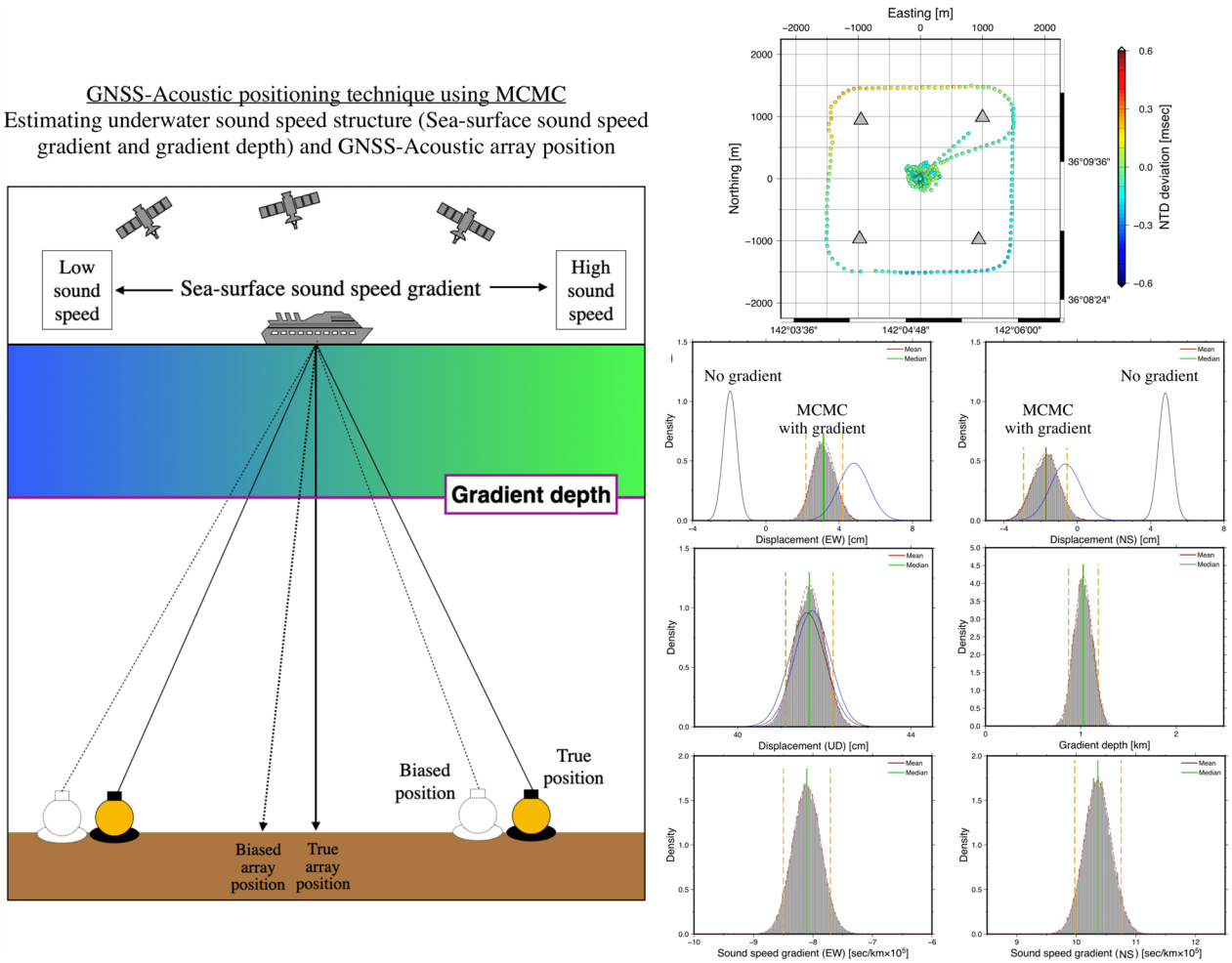

Introduction

Over the last 10 years, seafloor geodetic observational techniques, particularly the GNSS-acoustic (GNSS-A) technique, have provided important geophysical results and have been technically improved. The GNSS-A observational technique was contrived by Spiess (1985): a set of several (generally 3–6) seafloor transponders composes one GNSS-A site as a transponder array. GNSS-A positioning can be performed as a combination of GNSS positioning at a sea-surface platform and acoustic ranging between the sea-surface platform and seafloor transponders; seafloor displacement can be obtained as displacement of the transponder array, assuming that all seafloor transponders at each site move as a rigid body (referred to as the array positioning method). A basic GNSS-A positioning method was established around 2000, and it has shown geophysical observational results related to fault slips (e.g., coseismic slips and interplate coupling) in subduction zones (Spiess et al. 1998; Fujita et al. 2006; Kido et al. 2006; Ikuta et al. 2008). The importance of seafloor geodetic observations has been widely recognized since the occurrence of the 2011 Tohoku–Oki earthquake. The GNSS-A observations detected high coseismic displacements of over 30 m in the 2011 Tohoku–Oki earthquake (Kido et al. 2011; Sato et al. 2011), suggesting that a large coseismic fault slip of over 50 m reached the trench (Iinuma et al. 2012). After the 2011 Tohoku–Oki earthquake, GNSS-A observational networks around Japan were reinforced and provided a broad postseismic deformation pattern in the Tohoku region (Tomita et al. 2017;

Watanabe et al. 2021) and a spatial heterogeneity pattern of the interplate coupling in the Nankai region (Yokota et al. 2016). Recently, the GNSS-A positioning method has been improved by considering spatial heterogeneities in underwater sound-speed structures (Yasuda et al. 2017; Yokota et al. 2018a; Honsho et al. 2019; Watanabe et al. 2020). This accurate positioning method has enabled the discussion of various geophysical phenomena, such as slow-slip events, in detail (Honsho et al. 2019; Yokota and Ishikawa 2020).

The GNSS-A positioning methods have been performed by a linearized least squares method, because unknown parameters for seafloor transponder positions are non-linear. Most studies have used a classic iterative nonlinear least-squares (NLLS) method, such as the Gauss–Newton method, for conventional kinematic estimation (i.e., positioning for each acoustic ping, e.g., Spiess et al. 1998; Kido et al. 2006) and simple static estimation (i.e., positioning using a batch of acoustic pings, e.g., Honsho and Kido 2017). Meanwhile, some studies have introduced hyper-parameters for constraining the temporal fluctuation of the sound speed structure and optimized them using the Akaike Bayesian Information criterions (ABIC) (Akaike 1980) framework or trial-and-error (Ikuta et al. 2008; Watanabe et al. 2020). This approach is applicable under the assumption that each unknown parameter follows a Gaussian distribution, and it is difficult to consider the influence of the uncertainty of the hyper-parameters on the positioning errors.

Considering spatial sound speed heterogeneities, the recent GNSS-A positioning methods often assume a gradient structure of the sound speed. The sound speed gradient structure may be expressed by four parameters, which are often referred to as "shallow" and "deep" gradients, and each gradient has two components in the East–West (EW) and North–South (NS) directions (Yokota et al. 2018a; Honsho et al. 2019; Watanabe et al. 2020). Shallow gradients can easily be found as biased travel time residuals following the track of a sea-surface platform. The influence of shallow gradients on the travel time is a trade-off with temporal fluctuation of the sound speed as long as a single sea-surface platform is used (Honsho et al. 2019); therefore, their influence on the positions is not significant. However, the deep gradients cause biases of up to dozens of centimeters in the positioning results. The number of acoustic pings with various shot angles is critical for the estimation of the deep gradients (Honsho et al. 2019). Ideally, the deep gradients can be estimated using a transponder array with well-arranged over five transponders, even if a sea-surface platform stays at a fixed point (point survey) (Kido 2007; Tomita et al. 2019). However, most GNSS-A sites have only four transponders, and the estimation of the deep gradients using only point survey data is significantly affected by short-term and small-scale perturbations of the sound speed structure (Matsui et al. 2019). Therefore, it is important to use acoustic data when a sea-surface platform moves around (moving survey) to estimate deep gradients. Meanwhile, all GNSS-A campaign data do not necessarily include enough moving survey data because of sea conditions or observational objectives. Note that our previous studies mainly conducted the point survey for parts of the GNSS-A campaigns, because the point survey has numerically better positioning precision for horizontal components than the moving survey (e.g., Tomita et al. 2015, 2017). To analyze these data, Honsho et al. (2019) assumed that shallow sound speed gradient is continuously and constantly present up to a certain depth; in other words, the deep gradients are proportional to the shallow gradients with a proportional coefficient using a certain depth (hereafter referred to as the gradient depth). A similar approach was adopted by Yasuda et al. (2017) and Kinugasa et al. (2020). Although the gradient depth was fixed at approximately 500–1000 m in these studies, this value was not optimized according to the data. The gradient depth should be appropriately set, because this value functions as a type of hyper-parameter. However, since the gradient depth has a numerical limit (from zero to seafloor depth), this makes the optimization of gradient depth with a simple least squares method difficult.

In this study, we implement a Markov Chain Monte Carlo (MCMC) technique in the GNSS-A array positioning method (hereafter referred to as the MCMC-based array positioning method). The MCMC technique can flexibly provide posterior probability distributions of the unknown parameters without the Gaussian distribution assumption and can also estimate the uncertainties of hyper-parameters, similar to the other unknown parameters. Moreover, the MCMC technique easily provides the numerical limits of unknown parameters. These characteristics are expected to work well for the array positioning method including the gradient depth parameter. However, the MCMC-based array positioning method has a critical problem in terms of its computational cost. In GNSS-A positioning, we must perform travel time calculations for each acoustic ping. Because a travel time calculation technique requires an iterative acoustic ray-tracing technique with numbers of the sound speed layers, the computational cost of the MCMC technique is quite high. Thus, in this study, we developed a fast approximate travel time calculation technique and

implemented it in the MCMC-based array positioning method. We then applied the new method to actual observational data.

Method: approximate travel time calculation

In this section, we first introduce a conventional travel time calculation method as a reference for the approximate travel time calculation in "Introduction of exact travel time calculation" section. We then introduce two types of approximate travel time calculation methods in "Approximate travel time calculation" section. Their performance and parameter tuning are investigated in "Parameter optimization of the approximate travel time calculation" section.

Introduction of exact travel time calculation

In this section, we introduce a conventional travel time calculation method using the shooting method in a horizontally stratified sound-speed structure. This method considers Snell's law in a spherical frame. In this method, we approximate the Earth's shape around an observational site using a spherical Earth model with a local radius. This local Earth radius must naturally consider the acoustic ray azimuth angle of each acoustic ping to express the curvature of the ellipsoidal Earth (Chadwell and Sweeney 2010), and contributions of the azimuth angles require complex functions to our approximation approach. Meanwhile, Chadwell and Sweeney (2010) reported that approximate ellipsoidal Earth radii (such as local mean radius and Gaussian mean radius) generally provided ranging accuracy of < 1 mm for a few kilometers of the horizontal distance between the sea-surface and seafloor points without considering the azimuth angle contributions. Thus, we adopted the Gaussian mean radius as the local Earth radius for simplicity. The Gaussian mean radius is expressed as

$$R_G(\phi) = \sqrt{R_m(\phi)R_n(\phi)} \tag{1}$$

with

$$R_m(\phi) = \frac{a\left(1-e^2\right)}{\sqrt{\left(1-e^2\sin^2\phi\right)^3}}, \quad R_n(\phi) = \frac{a}{\sqrt{1-e^2\sin^2\phi}}. \tag{2}$$

where a, e, and ϕ are the semi-major axis, eccentricity of the ellipsoidal earth, and latitude, respectively.

We then formulated the travel time along path A–B, as shown in Fig. 1. The sound speed structure was given as N layers, and the sound speed and radius of the nth layer are denoted as v_n and r_n, respectively. Point A was located on the sea surface, whereas point B was located on the seafloor with an angular distance of Δ from point A. From Snell's law, we can obtain the ray parameter p as follows:

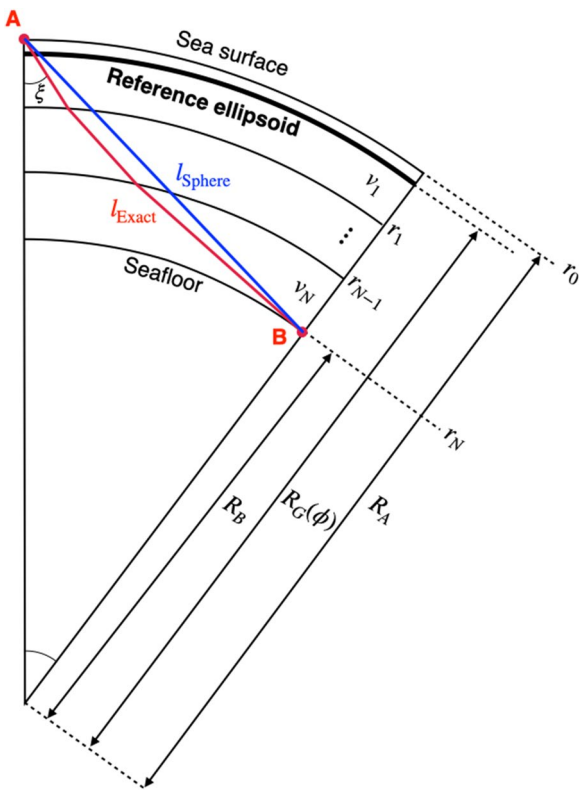

Fig. 1 Conceptional image of the acoustic path in this study. A horizontally stratified sound speed structure was assumed. Meanings of the characters are shown in the main text

$$p \equiv \frac{r}{v(r)}\sin\xi(r) \tag{3}$$

where $v(r)$ and $\xi(r)$ indicate the sound speed and ray angle at the radius of r. The ray parameter is preserved throughout the layers. The angular distance and travel time along path A–B can be calculated as follows:

$$\Delta_{\mathrm{cal}}(p) = \int \frac{\sin\xi}{r}\mathrm{d}l = \sum_{n=1}^{N}\int_{r_n}^{r_{n-1}} \frac{\tan\xi}{r}\mathrm{d}r \tag{4}$$

$$T_{\mathrm{cal}}(p) = \int \frac{1}{v_n}\mathrm{d}l = \sum_{n=1}^{N}\int_{r_n}^{r_{n-1}} \frac{1}{v_n\cos\xi}\mathrm{d}r \tag{5}$$

where dl is the infinitesimal distance along path A–B; then, $dl\cos\xi = dr$. Using Eq. 3 and considering v_n as constant in the corresponding layer, Eqs. 4 and 5 were rewritten using integral formulas as follows:

$$\Delta_{\mathrm{cal}}(p) = p\sum_{n=1}^{N} v_n \int_{r_n}^{r_{n-1}} \frac{1}{r\sqrt{r^2 - v_n^2 p^2}}\mathrm{d}r = \sum_{n=1}^{N}\left[\arccos\left(\frac{v_n p}{r_{n-1}}\right) - \arccos\left(\frac{v_n p}{r_n}\right)\right] \tag{6}$$

$$T_{\mathrm{cal}}(p) = \sum_{n=1}^{N}\frac{1}{v_n}\int_{r_n}^{r_{n-1}} \frac{r}{\sqrt{r^2 - v_n^2 p^2}}\mathrm{d}r = \sum_{n=1}^{N}\left[\sqrt{\left(\frac{r_{n-1}}{v_n}\right)^2 - p^2} - \sqrt{\left(\frac{r_n}{v_n}\right)^2 - p^2}\right]. \tag{7}$$

Since the positions of A and B were given, the angular distance could be obtained as follows:

$$\Delta = \frac{l_{\mathrm{AB}}}{R_G(\phi)} \tag{8}$$

where l_{AB} is the geodetic distance between A and B and is calculated as the horizontal distance in a local Cartesian coordinate by the transverse Mercator method. Thus, we could estimate the appropriate p using an iterative nonlinear least-squares method that minimizes $\Delta - \Delta_{\mathrm{cal}}$. Note that we assigned the initial value of p using Eq. 3 with the sound speed at the uppermost underwater layer, and then performed the Gauss–Newton method as the nonlinear least squares method. Using the appropriate p estimated by the nonlinear least squares method, we could obtain the precisely calculated travel time (hereafter referred to as T_{Exact}) using Eq. 7.

Approximate travel time calculation

Next, we developed a method to obtain an approximate travel time, T_{Appr}, reproducing T_{Exact}. First, we introduced "rough" travel time, T_{Sphere}, in the spherical coordinates without considering Snell's law. Denoting travel time in the vertical path (A, B in Fig. 1) as T_{vert}, it was calculated as follows:

$$T_{\mathrm{vert}} = \int_{R_{\mathrm{B}}}^{R_{\mathrm{A}}} \frac{1}{v(r)}\mathrm{d}r \tag{9}$$

where R_{A} and R_{B} are the Earth's radii at points A (sea surface) and B (seafloor), respectively. Assuming the ellipsoidal heights at points A and B to be h_{A} and h_{B}, respectively, $R_{\mathrm{A}} = R_G(\phi) + h_{\mathrm{A}}$ and $R_{\mathrm{B}} = R_G(\phi) + h_{\mathrm{B}}$ are obtained, respectively. Since h_{A} fluctuated from a certain height $\overline{h}_{\mathrm{A}}$ due to sea waves during an observational survey in the actual data, T_{vert} should be calculated for each acoustic ping in nature. However, integral calculation required significant calculation costs. Thus, we approximately calculate T_{vert} using δh which is defined as $\delta h = h_{\mathrm{A}} - \overline{h}_{\mathrm{A}}$:

$$T_{\mathrm{vert}} \approx \int_{R_{\mathrm{B}}}^{\overline{R}_{\mathrm{A}}} \frac{1}{v(r)}\mathrm{d}r + \frac{\delta h}{v(R_{\mathrm{B}})} \tag{10}$$

where $\overline{R}_{\mathrm{A}}$ is defined as $\overline{R}_{\mathrm{A}} = R_G(\phi) + \overline{h}_{\mathrm{A}}$. Thus, once we calculated the first term on the right-hand side of Eq. (10), the approximate T_{vert} could be easily calculated.

Then, travel time in the spherical coordinates could be calculated as follows:

$$T_{\mathrm{Sphere}} = \frac{T_{\mathrm{vert}}}{\cos\xi_{\mathrm{Sphere}}} = T_{\mathrm{vert}}\frac{l_{\mathrm{Sphere}}}{h_{\mathrm{A}} - h_{\mathrm{B}}}. \tag{11}$$

with

$$l_{\mathrm{Sphere}} = \sqrt{R_{\mathrm{A}}^2 + R_{\mathrm{B}}^2 - 2R_{\mathrm{A}}R_{\mathrm{B}}\cos\Delta} \tag{12}$$

As shown above, T_{Sphere} could be obtained by the simple calculation.

Then, we estimate the correction terms for T_{Sphere} to obtain the approximate travel time T_{Appr}. When the correction terms are expressed as a function f, T_{Appr} is defined as

$$T_{\mathrm{Appr}} = T_{\mathrm{Sphere}} + f \approx T_{\mathrm{Exact}}. \tag{13}$$

As shown in "Parameter optimization of the approximate travel time calculation" section, the correction terms can be obtained as polynomial functions of Δ and δh. We investigated two models of the correction terms: one includes Ith degrees of Δ (Model-1: f_1), and the other includes Ith degrees of Δ and δh (Model-2: f_2) as in

$$f_1 = \sum_{i=0}^{I} a_i \Delta^i \tag{14}$$

$$f_2 = \sum_{i=0}^{I} a_i \Delta^i + \sum_{i=0}^{I} b_i \Delta^i \delta h. \tag{15}$$

By assigning various values to I, we investigated the best pattern for the correction terms. Once the best pattern of the correction terms was determined, we could estimate the correction coefficients (a_i, b_i) for each seafloor transponder through a numerical test in advance as follows: (1) numbers of the synthetic observational points with various Δ and δh were prepared; (2) T_{Exact} and T_{Appr} for each seafloor transponder were calculated using the synthetic points; (3) the correction coefficients for each

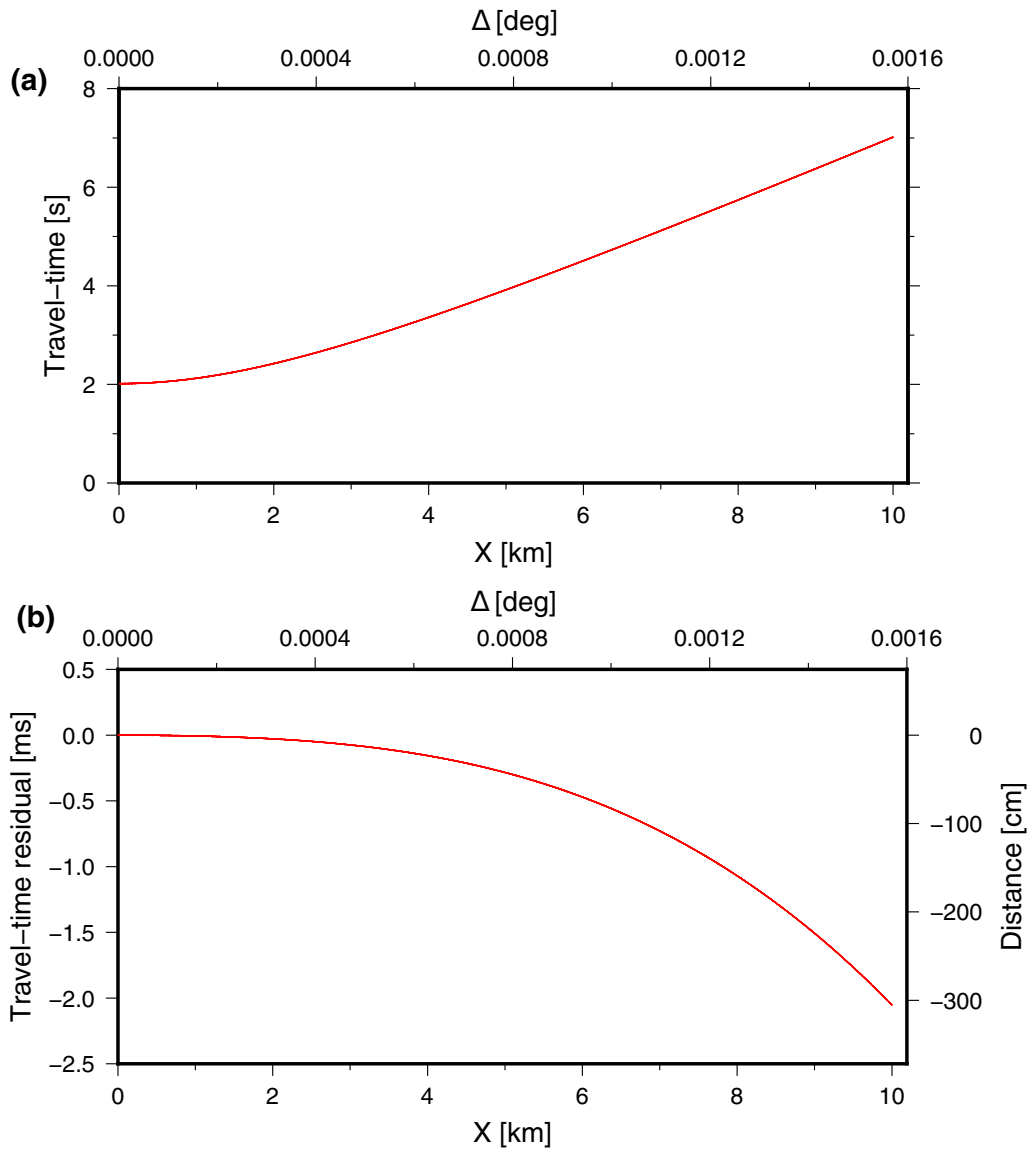

Fig. 2 Travel-times of the simulation data. **a** Simulated exact travel times. **b** Travel-time residuals that rough spherical travel times are subtracted from the exact travel-times

seafloor transponder were estimated by a simple least square method using $T_{\mathrm{Exact}} - T_{\mathrm{Appr}}$ as a data vector. After this optimization, we could calculate T_{Appr} that precisely reproduced T_{Exact} for a given Δ and δh using Eqs. 13–15 and the optimized correction coefficients. Although this method initially required calculation costs to optimize the correction coefficients, it could quickly calculate the approximate travel time after the initial optimization.

Parameter optimization of the approximate travel time calculation

Here, we investigate the optimal correction terms for the approximate travel time (Eqs. 13–15) and the performance of the approximate travel time calculation. Figure 2 shows the exact (T_{Exact}) and rough (T_{Sphere}) spherical travel times in a numerical simulation. We assumed a transponder with a depth of 3000 m and a

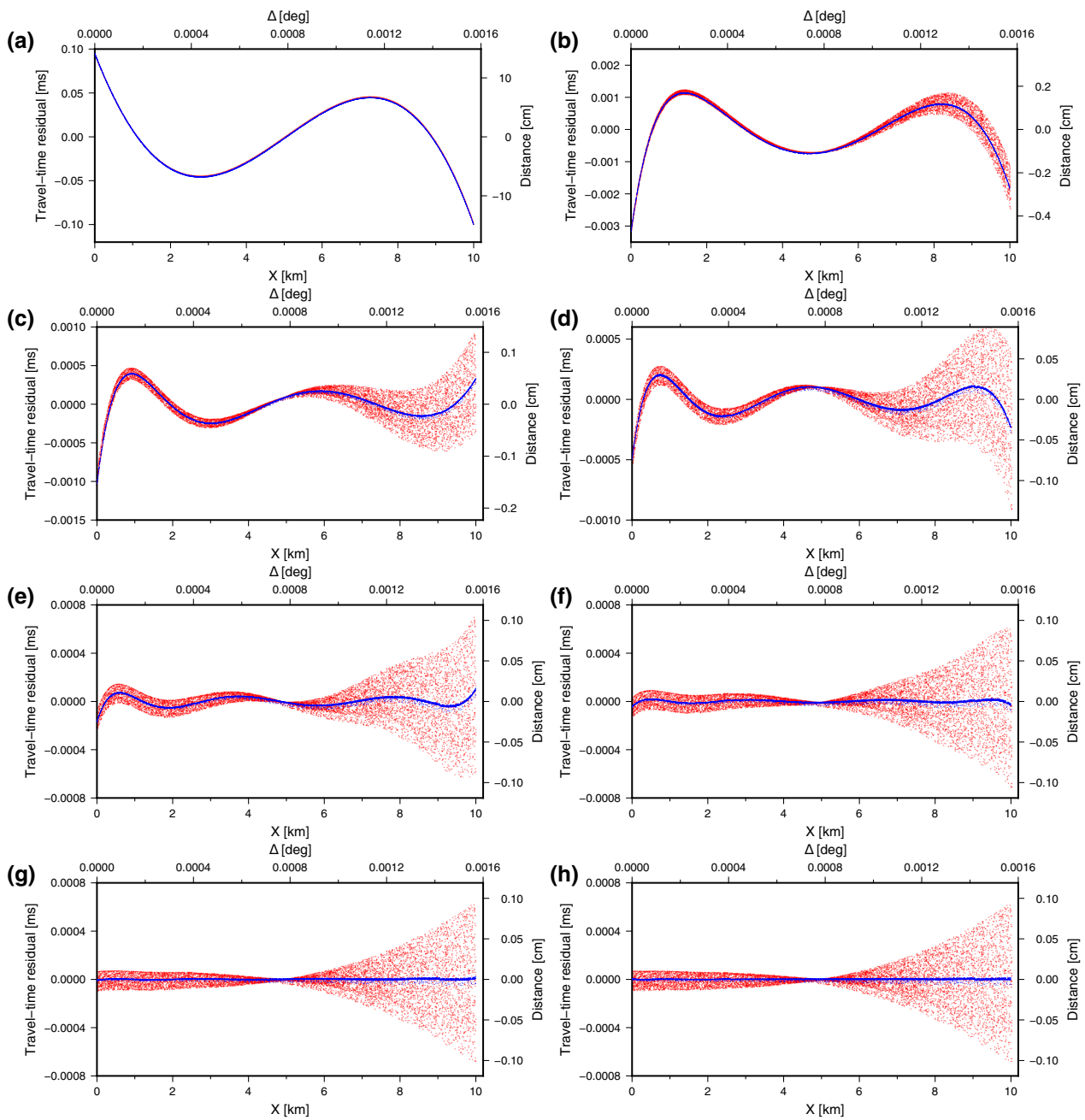

Fig. 3 Travel-time residuals for various travel-time approximation models. Red dots show travel time residuals for Model-1 (without height correction terms), and blue dots show those for Model-2 (with height correction terms). Each panel shows the travel time residuals for the two models with *l*th degrees of polynomial functions. **a** $l=1$, **b** $l=2$, **c** $l=3$, **d** $l=4$, **e** $l=5$, **f** $l=6$, **g** $l=7$, **h** $l=8$

horizontal position of zero (i.e., $X = 0$ m, $h = -3000$ m). Then, we calculated the exact and rough spherical travel times for the transponder from 10,000 sea-surface points randomly provided from a horizontal range of $0\,\text{m} \le X \le 10000$ m and a height of $-5\,\text{m} \le h \le 0\,\text{m}$. The height range imitates shaking of a sea-surface platform. A schematic of the numerical simulation is shown in Additional file 1: Fig. S2. A sound speed profile at the G10 site (143.483°E, 38.302°N, depth of 3271 m) produced from the average temperature and salinity models of WOA2018 (World Ocean Atlas 2018; Locarnini et al. 2018; Zweng et al. 2018) was used for the travel time calculation. The residuals of the travel times ($T_{\text{Exact}} - T_{\text{Sphere}}$) significantly increased depending on

the angular distance Δ, as shown in Fig. 2b. Considering this feature, we modeled the residuals using the polynomial functions of Δ as shown in Eqs. 13 and 14. The red dots in Fig. 3 denote the residuals using the I th degrees of polynomial functions (Model-1: $T_{\mathrm{Exact}} - T_{\mathrm{Sphere}} - f_1(I)$). The polynomial functions of Δ largely reduced the residuals; however, systematic residuals up to 0.2 cm remained even using higher degrees, such as in Fig. 3h, assuming $I = 9$. As indicated by the blue dots in Fig. 3, these systematic residuals can be reduced by the height correction terms using δh shown in Eq. (15) (Model-2: $T_{\mathrm{Exact}} - T_{\mathrm{Sphere}} - f_2(I)$). The RMS (root mean square) in Model-2 was approximately 0.01 mm, which was enough precision for the GNSS-A positioning.

We performed the same numerical simulations assuming different depths. Additional file 1: Table S1 summarizes the polynomial approximation results at depths of 1500 m, 3000 m, and 5000 m. In all cases, the RMS was approximately 0.01 mm in Model-2 with 8d polynomial functions. The Bayesian information criterion (BIC) (Schwarz 1978) did not necessarily show a minimum value in Model-2 with the 8d polynomial function, suggesting larger degrees. However, the precision was enough high; we employed Model-2 with 8d polynomial functions as the optimal model. To attain much higher ranging accuracy and precision, we need to consider the azimuth contribution to the travel time (discussed in "Introduction of exact travel time calculation" section) and to include its component to the approximation function f, shown in Eqs. 13–15. However, since the currently required accuracy is considered to be below 1 mm, because the other GNSS-A observational errors are further evident (e.g., GNSS positioning errors, sound speed structure bias, and bias of relative distance between a GNSS antenna and a sea-surface transducer), the performance of our current technique has enough accuracy and precision.

Moreover, to confirm the stability of Model-2 with 8d polynomial functions, we additionally calculated the approximate travel times for another set of randomly generated 10,000 sea-surface points using the coefficients for the 8d polynomial functions pre-determined above; then, we compared the approximate travel times with the exact travel times. This investigation was performed for the above three types of the depth (1500, 3000, 5000 m). As a result, the RMSs are almost same with those shown in Additional file 1: Table S1. Thus, our optimal approach (Model-2 with the 8d polynomial functions) can be stably performed without overfitting.

The practical procedure to obtain the approximate travel time T_{Appr} was as follows: (1) calculate $\bar{h}_{\mathrm{A}}$ by averaging the height component of the time-series of the sea surface transducer position; (2) generate numerical simulation data for each seafloor transponder, similar to the above numerical simulation in Fig. 2 (note that sea-surface points are generated from a horizontal range roughly within the water depth and a height range of ± 2.5 m from $\bar{h}_{\mathrm{A}}$); (3) estimate coefficients of the 8d polynomial function in Model-2 using a linear least-square method, (4) calculate the approximate travel time for the given actual sea-surface transducer position data using Eqs. 13 and 15 with the determined coefficients; (5) finally, once the coefficients for the polynomial functions are determined, calculate the approximate travel time for the given actual sea-surface transducer position data. Because $\bar{h}_{\mathrm{A}}$ is different among the observational cruises, the coefficients must be recalculated for each cruise and for each site.

Next, we investigated the performance of the approximate travel time by applying it to the actual observational data. The observational data were collected at the G10 site (water depth of ~ 3270 m) on November 4, 2016. The sea-surface vessel's track and initial sound speed profile are shown in Additional file 1: Fig. S3. Using these data, we performed a conventional GNSS-A array positioning by an NLLS method assuming a horizontally stratified sound speed structure in three types of travel time calculation methods: exact travel time, approximate travel time of Model-1 with the 4d polynomial function, and the approximate travel time of Model-2 with the 8d polynomial function. Details of the conventional GNSS-A array positioning method are introduced in "Introduction of the conventional NLLS-based GNSS-A positioning methods" section. The approximate travel time of Model-1 with the 4d polynomial function was only used for comparison, which is the simplest model among the investigated models with practical ranging precision (< 0.1 cm), as shown in Additional file 1: Table S1. The estimation results are summarized in Additional file 1: Table S2. The estimated position using the approximate travel time of Model-2 demonstrated almost the same values as those using the exact travel time. The difference between them was within approximately 0.01 mm. Therefore, our new travel time calculation method could be used for actual observational data with sufficient accuracy. The estimated position using the approximate travel time of Model-1 with the 4d polynomial function demonstrated about approximately 0.2 mm in difference in the height component. Although Model-1 with the 4d polynomial function was useful for practical use, we adopted Model-2 as the optimal model, because it demonstrated superior precision.

Finally, we confirmed the computational cost of the approximate travel time calculation technique. The computational costs vary depending on number of layers in the initial sound speed profile especially by the

conventional calculation technique (Exact travel-time calculation technique in "Introduction of exact travel time calculation" section). Here, we measured the computational times for our new technique and for the conventional technique using the above actual observational data at G10 on November 4, 2016. The initial sound speed profile for this site has 658 layers (5 m width for each layer). As a result, our new technique successfully reduced the computation time to 270 times less than the conventional technique. Note that this comparison did not consider the initial configuration of the coefficients for the polynomial functions. Because the initial configuration can be generally conducted for a minute, this initial configuration does not significantly affect for total calculation cost when performing the MCMC process.

Method: MCMC-based GNSS-A positioning method

We first introduce conventional GNSS-A array positioning methods using an NLLS technique assuming a horizontally stratified sound speed structure and a horizontally sloping sound speed structure in "Introduction of the conventional NLLS-based GNSS-A positioning methods" section, and we then present the MCMC-based array positioning method in "MCMC-based GNSS-A positioning method" section. The NLLS-based array positioning methods are introduced to validate the proposed method.

Introduction of the conventional NLLS-based GNSS-A positioning methods

Here, we introduce NLLS-based array positioning methods before formulating an MCMC-based GNSS-A positioning method. We first introduce an NLLS-based array positioning method assuming a horizontally stratified sound speed structure, and then introduce the assumption of a horizontally sloping sound speed structure.

Following Honsho and Kido (2017) and Tomita et al. (2019), the observation equation for the horizontally stratified sound speed structure for the nth shot to the kth seafloor transponder is expressed as follows:

$$\frac{1}{M\left(\xi_{k,n_k}\right)} T^{\mathrm{obs}}_{k,n_k} = \frac{1}{M\left(\xi_{k,n_k}\right)} T^{\mathrm{cal}}_{k,n_k}\left(\mathbf{p}_k + \delta\mathbf{p}; \mathbf{u}\left(t_{n_k}\right); v_0\right) + C_0\left(t_{n_k}\right) \tag{16}$$

with

$$M\left(\xi_{k,n_k}\right) = \frac{1}{\cos\xi_{k,n_k}}. \tag{17}$$

T^{obs}_{k,n_k} is the observed round-trip travel time and T^{cal}_{k,n_k} is the calculated round-trip travel time obtained in "Introduction of exact travel time calculation" and "Approximate travel time calculation" sections. The initial position of the kth seafloor transponder is denoted by $\mathbf{p}_k$, $\delta\mathbf{p}$ denotes the array displacement, $\mathbf{u}_{n_k}$ denotes the sea surface transducer position, and v_0 denotes the initial sound speed profile in the vertical direction. M indicates a normalizing factor which depends on the shot angles ξ_{k,n_k} and corresponds to a mapping function in GNSS positioning. The nadir total delay (NTD), which is indicated by $C_0\left(t_{n_k}\right)$, expresses the temporal fluctuation of the average sound speed at the time of the nth shot. Similar to Honsho and Kido (2017), we express the temporal fluctuation of the NTD by the superposition of cubic B-spline functions, Φ. Thus, using J number of cubic B-spline functions, $C_0(t)$ can be expressed as

$$C_0(t) = \sum_{j=1}^{J} c_j \Phi_j(t) \tag{18}$$

where c_j is a coefficient of the jth component of the cubic B-spline function. Defining $\tilde{T}^{\mathrm{cal}}_{k,n}$ using Eqs. 16–18 as

$$\frac{1}{M\left(\xi_{k,n_k}\right)} \tilde{T}^{\mathrm{cal}}_{k,n_k}(\delta\mathbf{p}, \mathbf{c}) = \frac{1}{M\left(\xi_{k,n_k}\right)} T^{\mathrm{cal}}_{k,n_k}(\delta\mathbf{p}) + \sum_{j=1}^{J} c_j \Phi_j\left(t_{n_k}\right), \tag{19}$$

the cost function can be written as

$$\sum_{k=1}^{K} \sum_{n_k=1}^{N_k} \left[\frac{1}{M\left(\xi_{k,n}\right)} \left\{ T^{\mathrm{obs}}_{k,n} - \tilde{T}^{\mathrm{cal}}_{k,n}(\delta\mathbf{p}, \mathbf{c}) \right\} \right] \rightarrow \text{minimize}, \tag{20}$$

where N_k and K indicate the total number of shots for the kth transponder and total number of seafloor transponders, respectively. Because the calculation of T^{cal}_{k,n_k} is nonlinear against $\delta\mathbf{p}$, this estimation of the unknown parameters is performed using the Gauss–Newton method, which is one of the most popular NLLS methods, as in Honsho and Kido (2017). To obtain reasonable solutions, J must have been optimized in advance. Because the total number of cubic B-spline functions expresses the roughness of temporal fluctuations of the average sound speed, the roughness potentially has a trade-off relationship with data misfits. Thus, we simply optimized J using BIC. We assumed that the residuals in Eq. 20 follow the Gaussian distribution and then calculate the likelihood to obtain the BIC.

Following Honsho et al. (2019), the observation equation in the horizontally sloping sound speed structure for the nth shot to the kth seafloor transponder is expressed as

$$\begin{aligned} \frac{1}{M\left(\xi_{k,n_k}\right)} T^{\mathrm{obs}}_{k,n_k} = {} & \frac{1}{M\left(\xi_{k,n_k}\right)} T^{\mathrm{cal}}_{k,n_k}\left(\mathbf{p}_k + \delta\mathbf{p}; \mathbf{u}\left(t_{n_k}\right); v_0\right) \\ & + C_0\left(t_{n_k}\right) + \mathbf{g}_{\mathrm{s}}(t_{n_k}) \mathbf{u}^{\mathrm{hor}}\left(t_{n_k}\right) \\ & + \mathbf{g}_{\mathrm{d}}(t_{n_k}) \mathbf{h}_{k,n_k} \end{aligned} \tag{21}$$

with

$$\mathbf{h}_{k,n_k} = \left(\tan\xi_{k,n_k}\sin\phi_{k,n_k}, \tan\xi_{k,n_k}\cos\phi_{k,n_k}\right) \tag{22}$$

where $\mathbf{g}_\mathrm{s}$ and $\mathbf{g}_\mathrm{d}$ indicate shallow and deep gradients, respectively. These terms contain the EW and NS components of the gradients, respectively. $\mathbf{u}^\mathrm{hor}$ indicates the horizontal component of $\mathbf{u}$, and ϕ is the azimuth of the acoustic path. Here, we assumed that the gradients were constant during the survey period (i.e., $\mathbf{g}_\mathrm{s}(t) = \tilde{\mathbf{g}}_\mathrm{s}$ and $\mathbf{g}_\mathrm{d}(t) = \tilde{\mathbf{g}}_\mathrm{d}$). Moreover, as long as a single sea surface platform is used, a trade-off relationship between the contributions of shallow gradients and the temporal fluctuation of NTD appears (Honsho et al. 2019). Therefore, we simultaneously expressed the temporal fluctuation of NTD and the contribution of the shallow gradients by the superposition of the cubic B-spline functions as follows:

$$C(t) = \sum_{j=1}^{J} c_j\Phi_j(t) \approx C_0(t) + \tilde{\mathbf{g}}_\mathrm{s}\mathbf{u}^\mathrm{hor}(t). \tag{23}$$

Defining $\tilde{T}^\mathrm{cal}_{k,n}$ using Eqs. 21–23 as

$$\frac{1}{M\left(\xi_{k,n_k}\right)}\tilde{T}^\mathrm{cal}_{k,n_k}\left(\delta\mathbf{p}, \mathbf{c}, \tilde{\mathbf{g}}_\mathrm{d}\right) = \frac{1}{M\left(\xi_{k,n_k}\right)}T^\mathrm{cal}_{k,n_k}(\delta\mathbf{p}) + \sum_{j=1}^{J} c_j\Phi_j\left(t_{n_k}\right) + \tilde{\mathbf{g}}_\mathrm{d}\mathbf{h}_{k,n_k}, \tag{24}$$

the cost function can be written as

$$\sum_{k=1}^{K}\sum_{n_k=1}^{N_k}\left[\frac{1}{M\left(\xi_{k,n}\right)}\left\{T^\mathrm{obs}_{k,n} - \tilde{T}^\mathrm{cal}_{k,n}\left(\delta\mathbf{p}, \mathbf{c}, \tilde{\mathbf{g}}_\mathrm{d}\right)\right\}\right] \rightarrow \text{minimize}. \tag{25}$$

Using the Gauss–Newton method, we could estimate the array position, temporal fluctuation of NTD, and deep gradients. The number of cubic B-spline functions J was set to be the same value, which is determined by the BIC of the inversion results, assuming a horizontally stratified sound speed structure.

MCMC-based GNSS-A positioning method

Using the fast travel time calculation technique described in "Approximate travel time calculation" section, we construct an MCMC-based GNSS-A positioning method. Following Honsho et al. (2019), we considered a case in which the deep gradient could not be directly estimated due to the data set quality (i.e., moving survey data were insufficient to directly solve the deep gradient, as described in "Introduction" section). In this case, we assumed that a shallow gradient $\tilde{\mathbf{g}}_\mathrm{s}$ was present up to the gradient depth D. According to Honsho et al. (2019), this model can provide the following relationship between the shallow and deep gradients:

$$\tilde{\mathbf{g}}_\mathrm{d} = \frac{D}{2}\tilde{\mathbf{g}}_\mathrm{s}. \tag{26}$$

Considering Eqs. 21 and 26, we could obtain the following observation equation:

$$\frac{1}{M\left(\xi_{k,n_k}\right)}T^\mathrm{obs}_{k,n_k} = \frac{1}{M\left(\xi_{k,n_k}\right)}T^\mathrm{cal}_{k,n_k}\left(\mathbf{p}_k + \delta\mathbf{p}; \mathbf{u}\left(t_{n_k}\right); \nu_0\right) + C_0(t) + \tilde{\mathbf{g}}_\mathrm{s}\mathbf{u}^\mathrm{hor}\left(t_{n_k}\right) + \frac{D}{2}\tilde{\mathbf{g}}_\mathrm{s}\mathbf{h}_{k,n_k}. \tag{27}$$

As indicated above, a trade-off relationship between the contributions of the shallow gradient $\tilde{\mathbf{g}}_\mathrm{s}\mathbf{u}^\mathrm{hor}$ and the temporal fluctuation of NTD $C_0(t)$ appeared; thus, it was difficult to directly estimate $\tilde{\mathbf{g}}_\mathrm{s}$ and $\mathbf{c}$ when $C_0(t)$ was modeled by cubic B-spline functions (Eq. 18). To cope with this issue, Honsho et al. (2019) modeled $C_0(t)$ as a combination of polynomial functions and cubic B-spline functions, which express the long-term and short-term fluctuations of NTD, respectively. They then introduced a hyper-parameter for suppressing the short-term fluctuation of NTD and optimized it using the ABIC framework (e.g., Yabuki and Matsu'ura 1992). This approach successfully extracted the contributions of a shallow gradient. However, in this method, it is necessary to introduce a large number of cubic B-spline functions; then, the variation of their coefficients is optimized by ABIC. In our method, number of the cubic B-spline functions is optimally reduced by BIC in advance as noted in "Introduction of the conventional NLLS-based GNSS-A positioning methods" section. This optimization is quite useful for fast computation through the MCMC method. Hence, we cannot directly utilize the approach of Honsho et al. (2019) to determine the shallow gradient. Here, we contrived a new approach similar to Honsho et al. (2019). To avoid introducing a hyper-parameter that constrains the short-term fluctuations of NTD in their approach, we propose the following two observation equations:

$$\frac{1}{M\left(\xi_{k,n_k}\right)}T^\mathrm{obs}_{k,n_k} = \frac{1}{M\left(\xi_{k,n_k}\right)}T^\mathrm{cal}_{k,n_k}(\delta\mathbf{p}) + \sum_{j=1}^{J} c_j\Phi_j\left(t_{n_k}\right) + \frac{D}{2}\tilde{\mathbf{g}}_\mathrm{s}\mathbf{h}_{k,n_k}, \tag{28}$$

$$\frac{1}{M\left(\xi_{k,n_k}\right)}T^\mathrm{obs}_{k,n_k} = \frac{1}{M\left(\xi_{k,n_k}\right)}T^\mathrm{cal}_{k,n_k}(\delta\mathbf{p}) + \sum_{m=0}^{4}\gamma_m t^m + \tilde{\mathbf{g}}_\mathrm{s}\mathbf{u}^\mathrm{hor} + \frac{D}{2}\tilde{\mathbf{g}}_\mathrm{s}\mathbf{h}_{k,n_k}. \tag{29}$$

Equation 28 models the temporal fluctuation of NTD $C_0(t)$ and the contribution of the shallow gradient $\tilde{\mathbf{g}}_s\mathbf{u}^{\mathrm{hor}}$ as cubic B-spline functions following Eq. 23, whereas Eq. 29 models the temporal fluctuation of NTD $C_0(t)$ as the long-term fluctuation of NTD by a quartic polynomial function. Therefore, Eq. 28 aims to solve the array displacement similar to Eqs. 24 and 25, and it treats $\delta\mathbf{p}$ and $\mathbf{c}$ as unknown parameters. On the other hand, Eq. 29 aims to extract the contribution of the shallow gradient, and it treats $\tilde{\mathbf{g}}_s$ and $\boldsymbol{\gamma}$ as the unknown parameters.

In the Bayesian approach, information on unknowns is expressed using a probability density function (PDF). According to Bayes' theorem (Bayes 1763), when data vector $\mathbf{d}$ is given, a posterior PDF for the unknown parameter vector $\mathbf{x}$ can be formulated as

$$p(\mathbf{x}|\mathbf{d}) = \frac{p(\mathbf{d}|\mathbf{x})p(\mathbf{x})}{p(\mathbf{d})} \propto p(\mathbf{d}|\mathbf{x})p(\mathbf{x}) \tag{30}$$

where $p(\mathbf{d}|\mathbf{x})$ indicates the likelihood for a given $\mathbf{x}$, $p(\mathbf{x})$ is a priori PDF of $\mathbf{x}$, and $p(\mathbf{d})$ is a priori PDF of $\mathbf{d}$. Since $p(\mathbf{d})$ indicates evidence and is independent of $\mathbf{x}$, the posterior PDF is propotional to $p(\mathbf{d}|\mathbf{x})p(\mathbf{x})$. In this study, we employed the Metropolis–Hastings algorithm (Metropolis 1953; Hastings 1970). This algorithm samples the posterior PDF from iterative calculations and is one of the most general algorithms for MCMC (Fukuda and Johnson 2008; Kubo et al. 2016). At each iteration step, we produced a candidate unknown parameter vector $\mathbf{x}'$ by adding perturbations to the unknown parameter vector of the previous step $\mathbf{x}$. In this study, we generated a perturbation for each unknown parameter from a uniform distribution with an individually constant step width. We then calculated the acceptance probability α as follows:

$$\alpha(\mathbf{x}'|\mathbf{x}) = \min\left[1, \frac{p(\mathbf{x}'|\mathbf{d})q(\mathbf{x}|\mathbf{x}')}{p(\mathbf{x}|\mathbf{d})q(\mathbf{x}'|\mathbf{x})}\right] \propto \min\left[1, \frac{p(\mathbf{x}'|\mathbf{d})}{p(\mathbf{x}|\mathbf{d})}\right], \tag{31}$$

where q denotes a proposal PDF. Because the proposal PDFs $q(\mathbf{x}|\mathbf{x}')$ and $q(\mathbf{x}'|\mathbf{x})$ are symmetric in this case, we could calculate the acceptance probability using the ratio of posterior PDFs. In our approach, we generated a random value u from a uniform distribution with a range of $[0, 1]$ and then accept the candidate when $\alpha(\mathbf{x}'|\mathbf{x}) > u$.

In this study, we assumed a uniform distribution with a range of $[-\infty, \infty]$ for the priori PDF of each unknown parameter except the gradient depth D. For the gradient depth, we assumed a uniform distribution with a range from 0 (sea-surface) to an observational site water depth. Thus, when the candidate gradient depth falls within this range, $p(\mathbf{x}) = 1$; otherwise, $p(\mathbf{x}) = 0$.

We calculated the likelihood $p(\mathbf{d}|\mathbf{x})$ by assuming that the data misfits followed a Gaussian distribution. Here, the data, residual, and unknown vectors are given as $\mathbf{d}_l$, $\mathbf{r}_l$, and $\mathbf{x}_l$, respectively. These vectors for Eq. 28 are provided as $l = 1$, whereas those for Eq. 29 are provided as $l = 2$. The residual vectors were obtained by subtracting the right-hand side from the left-hand side of Eqs. 28 and 29. The likelihood PDF for each equation is written as

$$p(\mathbf{d}_l|\mathbf{x}_l) = p(\mathbf{r}_l|\mathbf{x}_l) = \frac{1}{\sqrt{(2\pi)^N|\mathbf{C}_l|}}\exp\left(-\frac{1}{2}\mathbf{r}_l^{\mathrm{T}}\mathbf{C}_l^{-1}\mathbf{r}_l\right) \tag{32}$$

where $\mathbf{C}_l$ is a covariance matrix for each case and N is the total number of data given as $N = \sum_k^K N_k$. We introduced a scaling parameter, Λ_l, for each covariance matrix (Tomita et al. 2021) as follows:

$$\mathbf{C}_l = \begin{pmatrix} 10^{\Lambda_l}\sigma_0^2 & & 0 \\ & \ddots & \\ 0 & & 10^{\Lambda_l}\sigma_0^2 \end{pmatrix} \tag{33}$$

where σ_0 is the initial observational error, which is given as $\sigma_0 = 1.0 \times 10^{-4}[s]$. The scaling parameter is given as a power of 10 to promote efficient sampling (e.g., Kubo et al. 2016; Tomita et al. 2021). Including these scaling parameters, the unknown vectors are defined as $\mathbf{x}_1 = (\delta\mathbf{p}, \mathbf{c}, D, \Lambda_1)^{\mathrm{T}}$ and $\mathbf{x}_2 = (\tilde{\mathbf{g}}_s, \boldsymbol{\gamma}, \Lambda_2)^{\mathrm{T}}$.

The MCMC procedure used in this study is summarized in Additional file 1: Fig. S1. We first estimated $\delta\mathbf{p}$ and $\mathbf{c}$ by the NLLS-based positioning, assuming a horizontally stratified sound speed structure and also determined J using BIC, which are treated as initial values for the MCMC iteration ($\delta\mathbf{p}^{\mathrm{ini}}$, $\mathbf{c}^{\mathrm{ini}}$). Then, fixing the obtained $\delta\mathbf{p}^{\mathrm{ini}}$, we calculated the travel times for all data and obtained the following observation equation:

$$\frac{1}{M(\xi_{k,n_k})}T_{k,n_k}^{\mathrm{obs}} - \frac{1}{M(\xi_{k,n_k})}T_{k,n_k}^{\mathrm{cal}}\left(\delta\mathbf{p}^{\mathrm{ini}}\right) = \sum_{m=0}^{4}\gamma_j t^m + \tilde{\mathbf{g}}_s\mathbf{u}^{\mathrm{hor}}. \tag{34}$$

Because $\tilde{\mathbf{g}}_s$ and $\boldsymbol{\gamma}$ are linear parameters, this equation could be easily solved using the linear least-squares method. The obtained solutions were used as the initial values for the MCMC iteration ($\tilde{\mathbf{g}}_s^{\mathrm{ini}}$, $\boldsymbol{\gamma}^{\mathrm{ini}}$). We set the scaling parameters' initial values to zero, $\Lambda_1^{\mathrm{ini}} = \Lambda_2^{\mathrm{ini}} = 0$. Using these initial values for $\mathbf{x}_1$ and $\mathbf{x}_2$, we ran an MCMC iteration. If the number of iterations was odd, we provided perturbation in $\mathbf{x}_1$ and evaluated it based on the acceptance ratio. If the number of iterations was even, we provided perturbation in $\mathbf{x}_2$ and evaluate it based on the acceptance ratio. We performed 5×10^5 iterations and collected samples when the number of iterations was even and over the burn-in period (we set it to be 1×10^5).

Application of the MCMC-based array positioning method

In this section, the performance of the MCMC-based array positioning method using the approximate travel time of Model-2 with an 8d polynomial function by applying it to actual observational data. As shown in "MCMC-based GNSS-A positioning method" section, our method estimates the gradient depth, and moving survey data are essential (e.g., Honsho et al. 2019). Therefore, we employed observational data collected by the Japan Coast Guard (Watanabe et al. 2021) and investigated the performance of our method. We also applied our method to the observational data collected by Tohoku University (Tomita et al. 2017; Honsho et al. 2019, 2021). The data from Tohoku University included some campaigns without the moving survey data. We investigated the performance of our method on these observational data, which were considered unsuitable for solving underwater sound speed gradient structures. The spatial distributions of the GNSS-A observational sites employed in this study are shown in Additional file 1: Fig. S4. Moreover, we used conventional array positioning methods for comparison. Hereafter, we refer to our method and the conventional methods as the following: Method-1: the NLLS-based

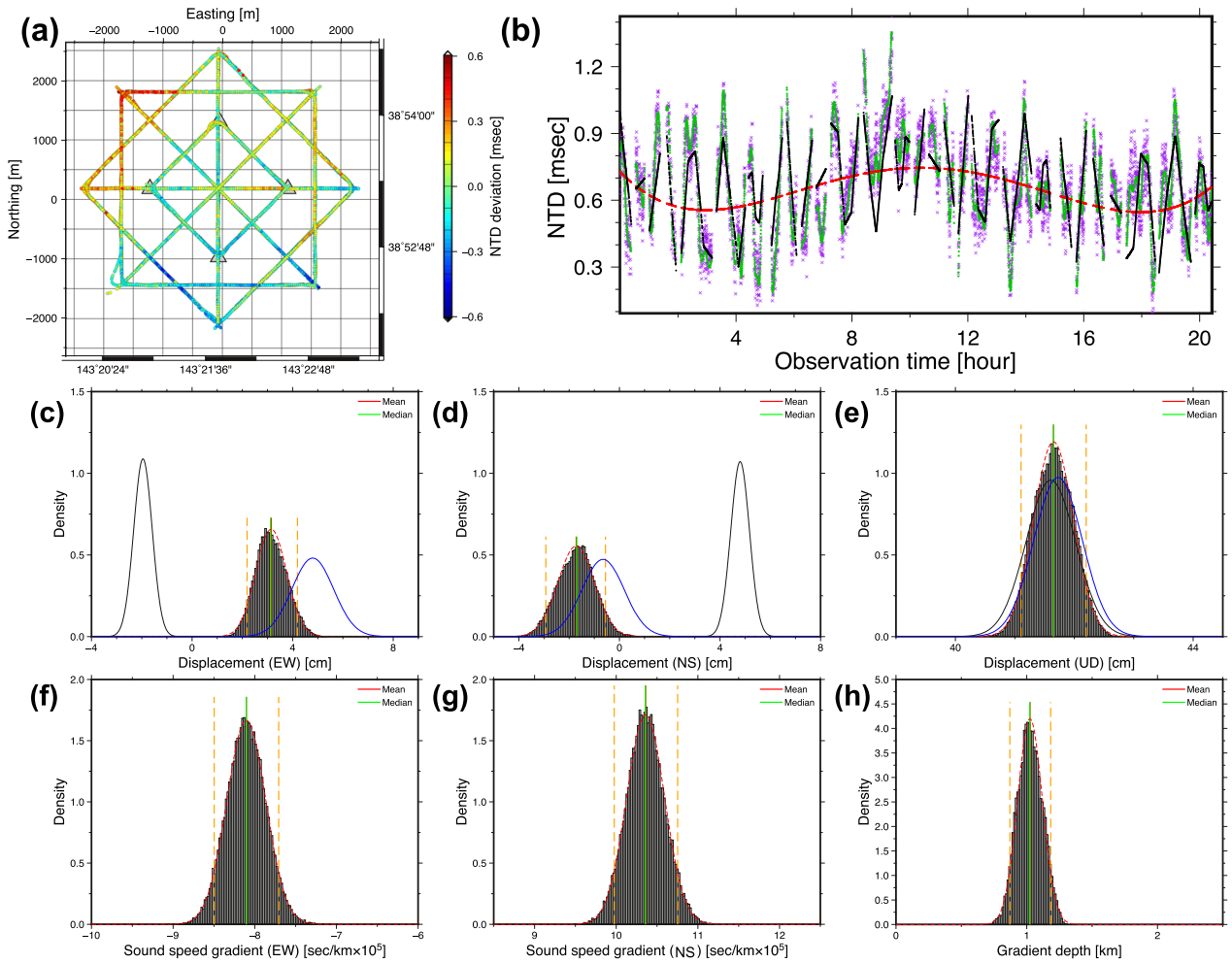

Fig. 4 Estimation results of Method-3 at KAMN on August 1, 2014. **a** Sea-surface platform positions when the acoustic signals were transmitted. The colors show NTDs subtracting the long-term fluctuation of NTDs estimated by Model-3. **b** NTD time-series. Purple plots show temporal fluctuation of NTD, the green curve shows the NTD modeled by the 3d B-spline functions, the red curve shows the long-term fluctuation of NTD modeled by the 4d polynomial function, and a black curve shows the NTD modeled by the long-term fluctuation and the shallow sound speed gradient. **c**–**h** posterior PDFs for the major unknown parameters: gray histograms demonstrate the PDFs obtained by Method-3, red curves show the Gaussian distributions equivalent to the PDFs of Method-3, black curves in **c**–**e** show the Gaussian distributions for the parameters estimated by Method-1, and blue curves in **c**–**e** show the Gaussian distributions for the parameters estimated by Method-2. The red, green, and orange vertical lines represent mean, median, and 95% credible interval

method assuming a horizontally stratified sound speed structure; Method-2: the NLLS-based method assuming a horizontally sloping sound speed structure; Method-3: the MCMC-based method estimating the gradient depth; Method-4: the MCMC-based method fixing the gradient depth of 600 m, similar to previous studies (Yasuda et al. 2017; Honsho et al. 2019; Kinugasa et al. 2020).

Application to GNSS-A data collected by Japan Coast Guard

Figure 4 summarizes the GNSS-A positioning results of the campaign on August 1, 2014, at KAMN site estimated by Methods 1–3. Figure 4a shows the entire track of this campaign, and Fig. 4b shows the travel time residuals in the nadir direction. In Fig. 4b, purple plots demonstrate the travel time residuals ($\frac{1}{M\left(\xi_{k,n_k}\right)}T^{\mathrm{obs}}_{k,n_k} - \frac{1}{M\left(\xi_{k,n_k}\right)}T^{\mathrm{cal}}_{k,n_k}$, as shown in Eqs. 28 and 29); the green curve shows the temporal fluctuation of NTD fitted by 3d B-spline functions ($\sum_{j=1}^{J} c_j \Phi_j\left(t_{n_k}\right)$, as shown in Eq. 28); the red curve shows the long-term fluctuation of NTD fitted by the 4d polynomial function ($\sum_{m=0}^{4} \gamma_m t^m$, as shown in Eq. 29), and the black curve shows a combination of the long-term fluctuation of NTD and the shallow gradient ($\sum_{m=0}^{4} \gamma_m t^m + \tilde{\mathbf{g}}_{\mathrm{s}}\mathbf{u}^{\mathrm{hor}}$, as shown in Eq. 29). The shallow gradient $\tilde{\mathbf{g}}_{\mathrm{s}}$ used in this figure was estimated using Method-3. As indicated in the "Method: MCMC-based GNSS-A positioning method" section, the shallow gradient was temporally constant, and Fig. 4b shows that the temporally constant shallow gradient can roughly express the spatial bias of the observed travel times. Since we employed the simple polynomial functions for modeling temporal fluctuation in Eq. (29), the fitness is relatively worse than Eq. (28) (see the black and green curves in Fig. 4b); however, we successfully extracted the spatial change depending on the shallow gradient in Eq. (29). This shallow gradient is also shown in Fig. 4a, where the color shows the on-the-spot NTDs subtracting the long-term NTD fluctuation, and the direction of the shallow gradients is roughly northwest. Although the introduction of a temporally varying shallow gradient might improve data fitting, these two factors show a trade-off relationship (e.g., Honsho et al. 2019). We considered the current technique to be adequate to stably obtain a temporally constant shallow gradient; however, a more sophisticated technique must be investigated in the future.

Figure 4c–h shows histograms of the MCMC sampling results for the major unknown parameters: the EW, NS, and UD (up-down) components of the array positions, the EW and NS components of the shallow gradients, and the gradient depth. All histograms are expressed as Gaussian distributions (equivalent Gaussian distributions are shown by dashed red curves), because absolute values of the skewness and kurtosis for these parameters are below 0.5; therefore, the assumption that an unknown parameter follows a Gaussian distribution in the conventional NLLS-based array positioning methods is suitable. However, note that the gradient depth occasionally shows a truncated Gaussian distribution when estimated close to the limits of the a-priori parameter range (i.e., depths of sea surface or of seafloor). In Figure 4c–e, we also describe Gaussian distributions for the array positions estimated by the NLLS-based array positioning methods (black and blue distributions show the results of Method-1 and Method-2, respectively). In this campaign cruise, the large offsets were caused in the both EW and NS components between Method-1 and Methods-2–3 (Figure 4c, d), while the UD positions were almost the same among these three positioning methods (Figure 4e). This suggests the sound speed gradient structure potentially affected the horizontal array positions. Method-2 directly estimated the deep gradient without any constraints, whereas Method-3 considered contributions of the gradient assuming that the deep gradient was linked to the shallow gradient. In spite of the difference among these methods, PDFs of the estimated positions in Method-2 and those in Method-3 were similar. Thus, the assumption that the deep gradient was linked to the shallow gradient was appropriate in this campaign.

To investigate the correlation relationship among the estimated parameters by Method-3, we described pair-plot of the major unknown parameters in Additional file 1: Fig. S5. This figure clearly shows strong correlation between the horizontal array positions and the gradient depth, whereas the up-down position and the shallow gradients were determined independently of the other parameters. This indicates that the direction of the sound speed gradient (the shallow gradients) is independently determined and that the intensity of the sound speed gradient is controlled by the gradient depth and affects the horizontal array positions.

To investigate the performance of our new method, we applied the above four array positioning methods to other campaign data collected by the Japan Coast Guard. Figure 5 shows a summary of the estimation results for all campaign data at KAMN distributed by Watanabe et al. (2021), and Additional file 1: Figs. S6–S10 show the estimation results for other sites of the Japan Coast Guard in the Tohoku region (KAMS, MYGI, MYGW, FUKU, and CHOS). Additional file 1: Fig. S11 shows a comparison of our results with the estimation results considering the sound speed gradients provided by the Japan Coast Guard (Yokota et al. 2018b). The estimation errors of the array positions by Method-1 and Method-2 are summarized in Additional file 1: Table S3, and the estimation

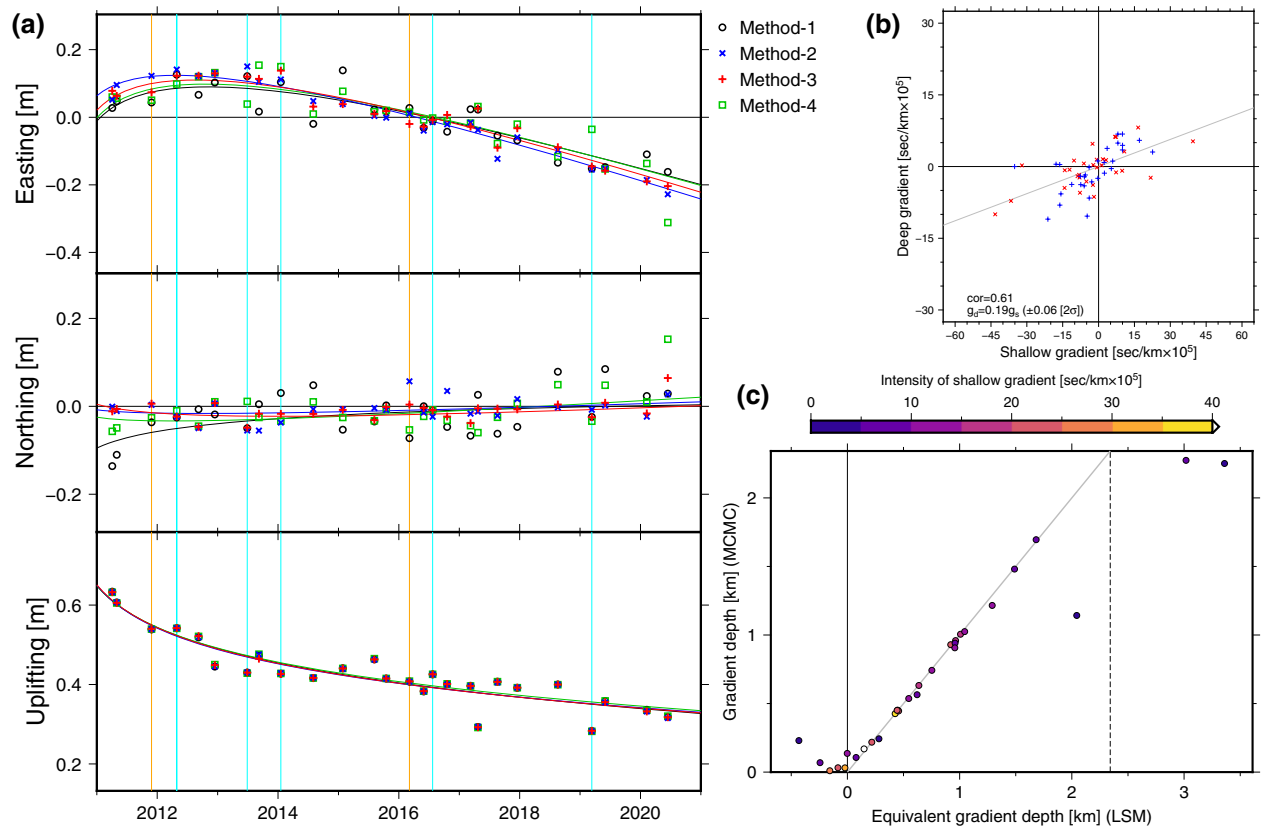

Fig. 5 Array positioning results at KAMN. **a** Time-series of the array positions. Open black circles, blue x-marks, red crosses, open green squares show the solutions estimated by Method-1, Method-2, Method-3, and Method-4, respectively. Cyan and orange vertical lines indicate the campaigns that the equivalent gradient depths are estimated to be lower than zero and larger than the seafloor depth, respectively. **b** Scatter diagram of the shallow gradients estimated by Method-3 and the deep gradients estimated by Method-2. Red and blue symbols represent EW and NS components, respectively. The solid line represents the linear regression line. The regression equation and the correlation coefficient are shown. **c** Scatter diagram of the equivalent gradient depths and the gradient depths estimated by Method-3. The colors of plots indicate the intensity of the shallow gradients estimated by Method-3. Solid and dashed vertical lines show the depths of zero and the seafloor

errors, skewness, and kurtosis of the array positions by Method-3 and Method-4 are summarized in Additional file 1: Tables S4 and S5, respectively.

Figure 5a and Additional file 1: Figs. S6a–S10a show time-series of the array positions estimated by Methods 1–4. We then estimated a fitting function of the array positions for each component and each method $d(t)$, where t is the time after the 2011 Tohoku–Oki earthquake, using the following equation:

$$d(t) = a_0 + a_1 t + a_2 \log\left(1 + \frac{t}{\tau}\right) \tag{35}$$

where a_0, a_1, and a_2 are estimation parameters, and τ is the relaxation time ($\tau = 0.787$ year, which was obtained by Fujiwara et al. 2022). The GNSS-A sites used in this study have showed significant contribution of the postseismic deformation of the 2011 Tohoku–Oki earthquake. Fujiwara et al. (2022) demonstrated that postseismic displacements of the onshore GNSS sites can be modeled using dual-logarithmic functions, and Watanabe et al. (2021) demonstrated that those of the offshore GNSS-A sites can be modeled using the single logarithmic function. Here, we estimated the fitting function using the single logarithmic function and assessed the robustness of the estimated array positions from the RMSs. The estimated fitting curves are shown in Fig. 5a and Additional file 1: Figs. S6a–10a, and the RMSs are summarized in Additional file 1: Table S6.

Figure 5a, Additional file 1: Figs. S6a–S10a and Additional file 1: Table S6 clearly demonstrate that Method-2 and Method-3 provided temporally stable solutions (the RMSs are ~3 cm) compared to Method-1 (the RMS is ~5 cm) and Method-4 (the RMS is ~4 cm) in the horizontal components. Moreover, there is no clear difference for the up-down component among the estimation methods. These results suggest that the accuracy of our new method (Method-3) is compatible with that of

Method-2, suggesting that appropriate consideration of the sound speed gradients is important for obtaining robust solutions. Note that Method-3 is also compatible with Yokota et al. (2018b) (Additional file 1: Fig. S11). Although the estimation errors in Method-1 (~0.4 cm in Additional file 1: Table S3) are generally smaller than those in Method-2 (~0.9 cm in Additional file 1: Table S3) and Method-3 (~0.6 cm in Additional file 1: Table S4), Method-1 provided relatively lower accuracy than the other methods (Additional file 1: Table S6). This suggests that the solutions of Method-1 contain the systematic errors due to the horizontal heterogeneity of the sound speed structure and failed to evaluate them in the estimation errors shown in Additional file 1: Table S3. Since Method-2 and Method-3 consider the sound speed gradients, their estimation errors are generally larger than Method-1. Although Method-4 considers the sound speed gradients, the estimation errors of Method-4 are comparable with Method-1 (~0.4 cm in Additional file 1: Table S5). This is because the intensity of the sound speed gradients (i.e., the gradient depth) was fixed.

Here, we examined the assumption of Method-3 that the deep gradient is linked to the shallow gradient. Figure 5b shows the relationship between the shallow gradients obtained as the initial values for Method-3 $\tilde{\mathbf{g}}_s^{\mathrm{ini}}$ and the deep gradients estimated by Method-2 for all campaigns at KAMN. Figure 6 shows a compilation of the shallow and deep gradient scatter plots of for all sites (Figure 5b and Additional file 1: Figs. S6b–S10b). Note that the shallow gradients $\tilde{\mathbf{g}}_s^{\mathrm{ini}}$ are obtained independently of the deep gradients. If the assumption was appropriate, these parameters should show positive correlation, as expressed by Eq. 26 (Honsho et al. 2019). Then, we calculated correlation coefficients for these scatter plots. As a result, the positive correlation was found for all sites (correlation coefficients of ~0.36–0.86). Moreover, we also calculated a linear regression line for each scatter plot without including an intercept. Then, we obtained significant positive proportional relationship between the shallow and the deep gradients (proportional coefficients of ~0.11–0.46, which corresponds to the gradient depths of ~0.22–0.92 km as derived from Eq. 26). Since the gradient depth is not a constant value among the campaigns, the scatter plots do not necessarily demonstrate strict linear relationship. Therefore, each proportional coefficient might represent an average gradient depth for the corresponding site. These findings show the positive correlation between the shallow and the deep gradient and support the validity of the assumption of Method-3 on actual observational data. Furthermore, we confirmed that the shallow gradients estimated by Method-3 were almost same with their initial values $\tilde{\mathbf{g}}_s^{\mathrm{ini}}$; thus, the shallow gradients can be constrained by Eq. (29) independently of the assumption.

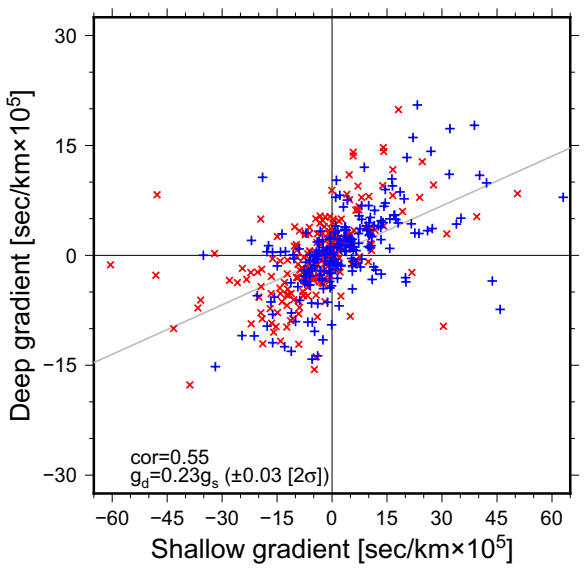

Fig. 6 Scatter diagram of the shallow gradients and the deep gradients for the six sites. The shallow gradients were estimated using Method-3, and the deep gradients were estimated using Method-2. Red and blue symbols represent EW and NS components. The solid line represents the linear regression line. The regression equation and the correlation coefficient are shown

We then examined the degree of the gradient depth in the actual ocean from the estimation results. Figure 5c and Additional file 1: Figs. S6c–S10c show the gradient depths estimated by Method-3 and the equivalent gradient depths calculated from the deep gradients of Method-2. The equivalent gradient depth can be obtained by the following process: we first calculated a gradient depth for each horizontal component using Eq. 26 with the shallow gradient of Method-3 and the deep gradient of Method-2; we then calculated the mean of these two gradient depths weighted by the intensity of the shallow gradients (i.e., absolute values of the EW and NS shallow gradients) as the equivalent gradient depth. In these figures, the equivalent gradient depths generally coincide with the gradient depths of Method-3, suggesting the validity of the linear relationship between shallow and deep gradients. The equivalent gradient depths for most campaigns fall within the estimation range of the gradient depth in Method-3 which was introduced as a physical restriction (i.e., from zero to a water depth). Meanwhile, the equivalent gradient depths for several campaigns were outside this physically restricted range. These campaigns are indicated by the cyan and orange vertical lines in Figure 5a and Additional file 1: Figs. S6a–S10a, which indicate campaigns with an equivalent gradient depth lower than zero and larger than the water depth,

respectively. The equivalent gradient depth presupposes a simplified sound speed structure (uniform sound speed gradient from the sea-surface to the gradient depth). Therefore, it would occasionally demonstrate an unphysical depth when a complex sound speed structure exists. If a strong sound speed heterogeneity exists only in a deep portion, the equivalent gradient depth would exceed the water depth. If directions of the shallow and deep sound speed heterogeneities are remarkably different, the equivalent gradient depth would be negative. When the equivalent gradient depth was lower than zero, the absolute values of the gradient depth of Method-3 and the equivalent gradient depth were generally small, that is, the deep gradient was estimated to be small. In this case, the influence of the sound speed gradient on the positions was small, and the difference between Method-2 and Method-3 was also small. However, when the equivalent gradient depth was larger than the water depth, differences of up to 10 cm between Method-2 and Method-3 were occasionally found. Because the intensity of shallow gradients among these campaigns was generally low (color of Figure 5c and Additional file 1: Figs. S6c–S10c), the sound speed structures of these campaigns might be exceptional, which the deep gradients were much larger than the shallow gradients. Although such differences were found between Method-2 and Method-3, it was difficult to determine whether Method-2 or Method-3 was more plausible based on the stability of the time series of the array displacements.

From the above findings, our assumption used in Method-3 was appropriate; accuracy of Method-3 was compatible with that of Method-2, which directly estimates the deep gradients. Figure 5a and Additional file 1: Figs. S6a–S10a show Method-4, which considered the sound speed gradient with a fixed gradient depth and corresponds to the methods of some previous studies (e.g., Yasuda et al. 2017; Honsho et al. 2019; Kinugasa et al. 2020). Method-4 generally demonstrated better solutions than Method-1 did; however, these solutions are much more unstable than the solutions of Method-2 and Method-3. This suggested that the gradient depths should be optimized for each campaign. However, Method-4 showed improved solutions as along with Method-2 and Method-3 at the CHOS site (Additional file 1: Fig. S10a). As shown in Additional file 1: Figs. S10b and S10c, the sound speed sloping structure at this site was almost constant among the campaigns, and the gradient depth was also constantly determined as approximately 0.5–1 km. Moreover, number of the equivalent gradient depth under unphysical range is quite smaller than the other site. Accordingly, the fixed gradient depth (0.6 km) in Method-4 worked well for this site. This constant sound-speed sloping structure might have been caused by the Kuroshio Current, which is constantly present over this site, and a complex sound speed structure might not tend to be caused compared with the other sites. Therefore, Method-4 was effective for such exceptional sites or when a gradient depth could be derived from other underwater measurements (Kinugasa et al. 2020), but it is plausible to optimize the gradient depth for diverse cases.

Application to campaign data collected by Tohoku University

Figure 7 summarizes the GNSS-A positioning results of the campaign on November 13, 2015, at the G20 site estimated by Methods-1–3. The pair-plots of the posterior PDFs estimated by Method-3 are shown in Additional file 1: Fig. S12. Including this campaign survey, a survey track for each site of Tohoku University was composed of a short-term moving survey (e.g., during approximately 0–2 h in Fig. 7b) and a long-term point survey (e.g., during approximately 2–14 h in Fig. 7b). As shown in Figure 7a, b, f, g, the shallow gradient was determined from the short-term moving survey data, with a direction of northwest. In this campaign, the gradient depth was roughly determined as a Gaussian distribution (Fig. 7h), and the differences in the array displacements between Method-1 and Method-3 reached several centimeters. Method-2 also provided similar solutions as Method-3; thus, such small amounts of moving data had the potential to detect a sound-speed sloping structure.

Figures 8, 9, and 10 show the time series of the array displacements and sea-surface tracks for campaigns at G20, G17, and G10, respectively. We conducted moving surveys for all campaigns at G20 (Fig. 8). Although the moving survey data were expected to be useful for estimating a sound-speed sloping structure and vertical motions, the solution of TB12-01 showed a clear bias in the vertical component using all methods and a large bias in the horizontal component using Method-2. These anomalies of TB12-01 at G20 were considered to have occurred because of the low signal-to-noise ratio of the acoustic data in this campaign. Aside from these anomalies, Method-2 demonstrated temporally irregular motions compared with Method-3 in Figure 8, possibly meaning that Method-2 failed to provide stable solutions for most campaign data of Tohoku University. As Honsho et al. (2019) pointed out, it is difficult to robustly solve a sound speed structure using Method-2. In contrast, Method-3 successfully provided robust solutions because of the following two factors: (1) Method-3 practically reduced unknown parameters. Although Method-2 estimated two gradient parameters for the sound-speed sloping structure: the deep gradients for the EW and NS components, Method-3 estimated a single gradient

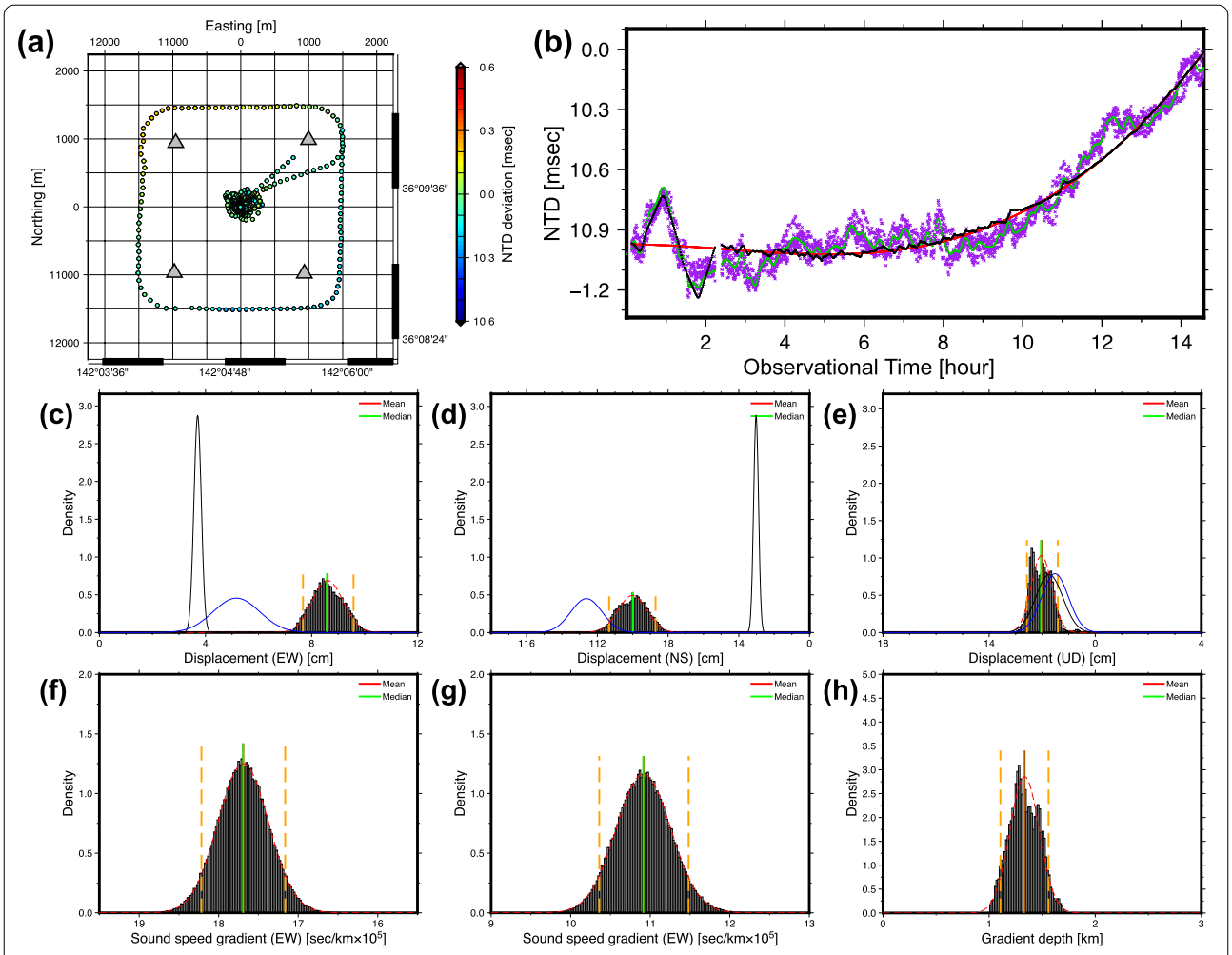

Fig. 7 Estimation results of Method-3 at G20 on November 13, 2015. Each panel is described in the same manner as in Fig. 4

parameter: the gradient depth (note that the shallow gradients were almost independently solved in Method-3). (2) Method-3 employed a constraint on the range of the gradient depth, which prevented physically unnatural solutions. However, it was difficult to estimate the gradient parameters even with Method-3 when a moving survey was lacking. No moving surveys were conducted during campaigns of D3K15-01, YK16-02, KS-16-14, and KS-17-13 at G17 (campaigns with vertical gray lines in Fig. 9a). Among these campaigns, the solutions assuming a sound-speed sloping structure (Methods-2, -3, and -4) were temporally violated; thus, these methods were not appropriate for data application without a moving survey. For these cases, the conventional positioning method assuming a horizontally stratified sound speed structure (Method-1) was appropriate for obtaining stable positions.

Finally, we presented a special case to detect a sound-speed sloping structure at a site with multi-angled transponders, for example, at G10 (Fig. 10). Tohoku University has adopted multi-angled transponder geometry at some GNSS-A sites, allowing us to obtain acoustic data with multiple shot angles even through a point survey (Tomita et al. 2019). The GNSS-A site with multi-angled transponders could theoretically solve vertical motions and gradient parameters without moving survey data (e.g., Kido 2007; Tomita et al. 2019; Matsui et al. 2019). Because of this benefit, Methods-2 and -3 successfully provided robust solutions, even for campaigns without moving survey data (campaigns with vertical gray lines in Fig. 10a). Moreover, unlike G17 and G20, Method-2 and Method-3 provided temporally stabilized motions for most campaigns. This also reflected the utility of multi-angled transponders. Considering that it was naturally impossible to properly estimate shallow gradients without moving survey data, Methods-3 and -4 did not work well among these campaigns, even if these methods

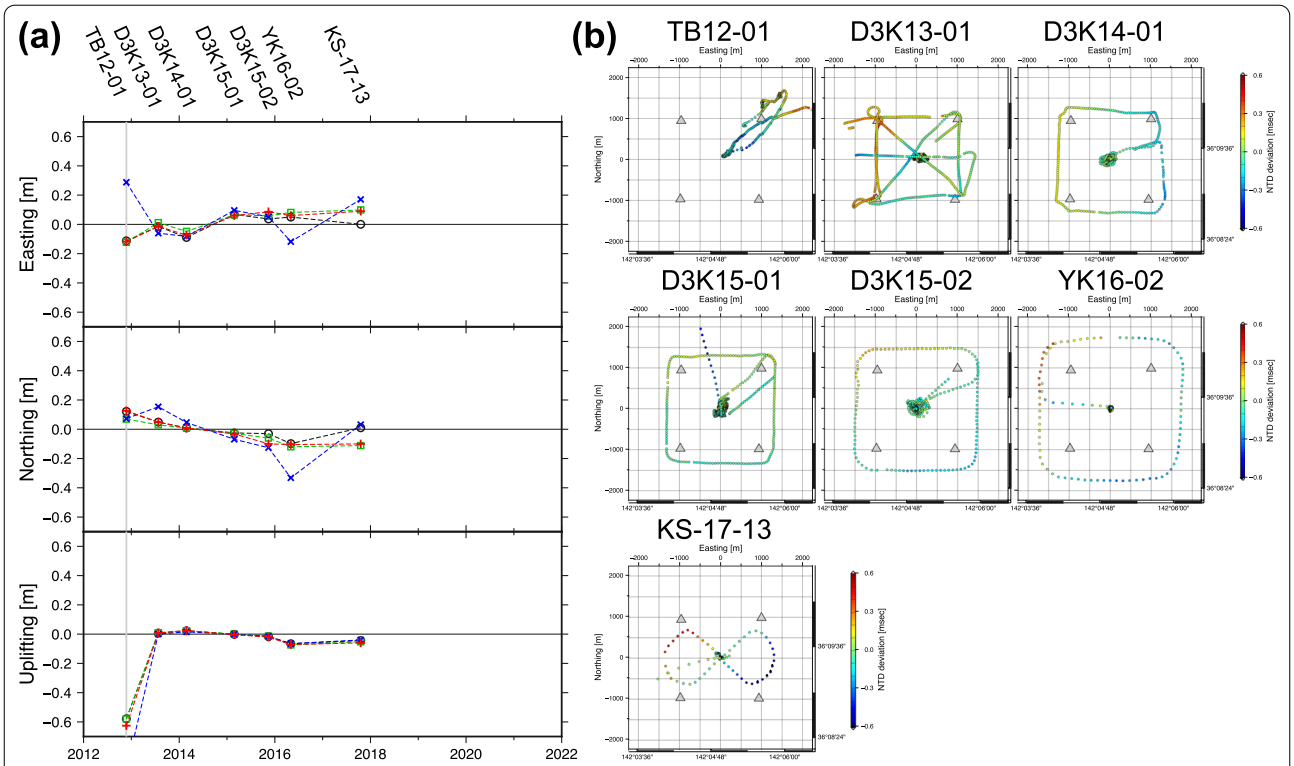

Fig. 8 Time-series of the array positions and sea-surface tracks for campaigns at G20. **a** Time-series of the array positions. Open black circles, blue x-marks, red crosses, open green squares show the solutions estimated using Method-1, Method-2, Method-3, and Method-4, respectively. **b** Sea-surface platform positions when the acoustic signals were transmitted. The colors show NTDs subtracting the long-term fluctuation of NTDs estimated by Model-3

numerically solved the gradient parameters. Therefore, Method-2 was the most appropriate method for processing the observation data of multi-angled transponder sites. However, as claimed by Matsui et al. (2019), a long observational period is required to eliminate the contributions of a shallow sound-speed gradient using only point survey data at a multi-angled transponder site; therefore, if the observational time was not sufficiently long, Method-1 was preferred.

Conclusions and discussion

In this study, we developed an approximate calculation technique for rapidly calculating travel times, and then, using this technique, we developed a new GNSS-A array positioning method using an MCMC technique. In the approximate travel time calculation technique, we first calculated the approximate travel time by a simple geometric computation and then corrected it using the 8th degrees of polynomial functions of an angular distance and the height of a sea-surface platform. The correction terms must be optimized in advance suing numerical simulations. Conventional travel time calculation techniques in a horizontally stratified sound speed structure which consider Snell's law were exact but required too long a calculation time to perform the MCMC technique. The approximate calculation technique can rapidly provide travel times (the new technique reduces the computation time to ~ 270 times less than the conventional technique) with enough accuracy and precision in array position estimation. The computational cost of the MCMC-based array positioning method depends on the data quantity; however, for example, it took 30 min to perform our MCMC method with 5×10^5 iterations for the actual observational data on August 1, 2014 at KAMN (the results are shown in Fig. 4).

The MCMC-based array positioning method estimated the gradient depth and array positions, assuming a horizontally sloping sound speed structure. In a horizontally sloping sound speed structure, shallow and deep gradients could be defined, and the deep gradient provided a significant bias in the horizontal array position. In our method, we assumed that a sound speed gradient was constantly present from the sea surface to the gradient depth, that is, the deep gradient was proportional to the

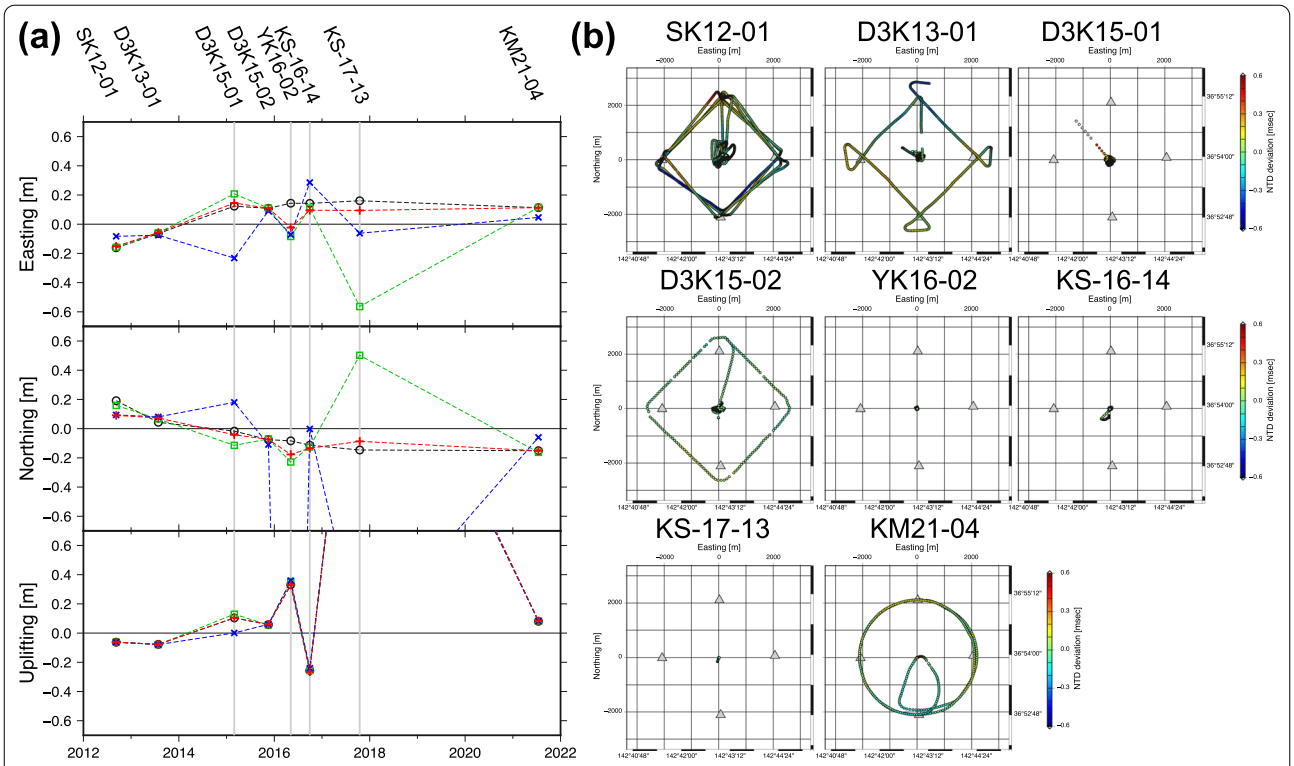

Fig. 9 Time-series of the array positions and sea-surface tracks for campaigns at G17. Each panel is described in the same manner as in Fig. 8

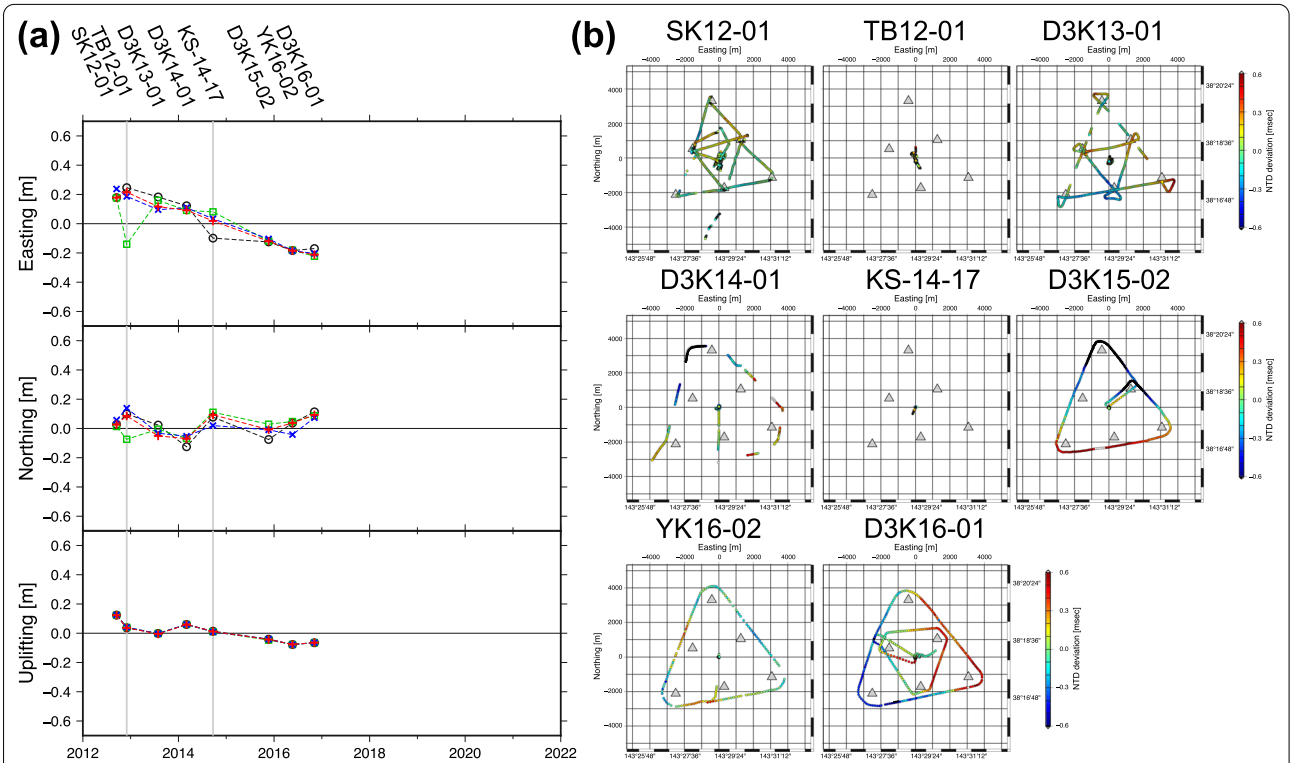

Fig. 10 Time-series of the array positions and sea-surface tracks for campaigns at G10. Each panel is described in the same manner as in Fig. 8

shallow gradient, and the gradient depth corresponded to a proportionality coefficient. It was plausible to directly estimate the deep gradient using the amount of moving survey data (e.g., Yokota et al. 2018a; Watanabe et al. 2021); however, when the moving survey data were insufficient, the pseudo deep gradient was obtained from the shallow gradient through this assumption (e.g., Yasuda et al. 2017; Honsho et al. 2019; Kinugasa et al. 2020). In previous studies, the generality of this assumption was not well-investigated, and optimization of the gradient depth was not performed.

We applied the MCMC-based array positioning and the conventional array positioning methods on the actual observational data collected by the Japan Coast Guard, which contain sufficient moving survey data. The following findings were obtained:

1. Our new method generally demonstrated Gaussian distributions for PDFs of unknown parameters, whereas the PDF of gradient depth occasionally showed a truncated Gaussian distribution. Namely, the array positioning could be performed using the framework of the least-squares method; however, it was plausible to perform an MCMC technique when the range of an unknown parameter could be physically restricted, as was the case of the gradient depth.
2. Our new method provided robust solutions for the array positions compared with those estimated by a conventional array positioning method by assuming a horizontally stratified sound speed structure; it was comparable with the conventional method that directly estimated the deep gradient assuming a horizontally sloping sound-speed structure.
3. The deep gradients generally showed a proportional relationship with shallow gradients. Thus, our assumption that a sound speed gradient exists from the sea surface to the gradient depth was valid.

Next, we applied our method to actual observational data collected by Tohoku University, which contained small amounts of moving survey data or no moving survey data. The following findings were found:

1. When compared to the traditional array positioning method assuming a horizontally stratified sound structure, our new method stably obtained a truncated Gaussian distribution as the PDF of the gradient depth and demonstrated that a temporally robust time-series of the array positions was obtained in the case of observational data containing small amounts of moving survey data. Therefore, small amounts of moving survey data had the potential to detect horizontal gradients to a certain degree.
2. It was difficult to directly estimate the deep gradient using the conventional method, assuming a horizontally sloping sound speed structure from small amounts of moving survey data. In contrast, our new method made more robust estimations than the conventional method did, because it practically reduced the numbers of unknown parameters modeling the horizontally sloping sound speed structure, and also due to the introduction of physical restriction on the gradient depth.
3. Even with our new method, we could not detect a horizontally sloping sound speed structure from actual observational data without moving survey data. In this case, the conventional array positioning method is preferred, assuming a horizontally stratified sound structure. However, it should be noted that deep gradients could be directly estimated for a multi-angled transponder site if the observational time is sufficiently long.

As the above findings show, our new method successfully optimizes the gradient depth, and is, therefore, an effective technique to model an underwater sloping sound speed structure and robustly obtains array positions, except in the case in which no moving survey data is available.

Abbreviations

ABIC: Akaike Bayesian information criterion; BIC: Bayesian information criterion; GNSS: Global Navigation Satellite System; GNSS-A: GNSS-acoustic; MCMC: Markov Chain Monte Carlo; NLLS: Non-linear least-squares; NTD: Nadir total delay; PDF: Probability density function.

Supplementary Information

The online version contains supplementary material available at https://doi.org/10.1186/s40623-022-01740-0.

Additional file 1. Fig. S1: Flowchart of an MCMC procedure in this study. **Fig. S2**: Schematic image of the numerical simulation in "Method: MCMC-based GNSS-A positioning method" section. **Fig. S3**: Track of the observational vessel and the sound speed profile used in "Method: MCMC-based GNSS-A positioning method" section. **Fig. S4**: Distribution of the GNSS-Acoustic sites employed in this study. **Fig. S5**: Pair-plots of the posterior PDFs at KAMN on August 1, 2014. **Fig. S6**: Array positioning results at KAMS. **Fig. S7**: Array positioning results at MYGI. **Fig. S8**: Array positioning results at MYGW. **Fig. S9**: Array positioning results at FUKU. **Fig. S10**: Array positioning results at CHOS. **Fig. S11**: Time series of the array position at Japan Coast Guard sites. **Fig. S12**: Pair-plots of the posterior PDFs at G20 on November 13, 2015. **Table S1**: Numerical simulation results for the approximate travel-time calculation model. **Table S2**: Positioning results in "Method: MCMC-based GNSS-A positioning method" section. **Table S3**: Standard deviation of the array positions estimated by Method-1 and Method-2. **Table S4**: Standard deviation, skewness, and kurtosis of the array positions estimated by Method-3. **Table S5**: Standard deviation, skewness, and kurtosis of the array positions estimated by Method-4. **Table S6**: RMSs between the estimated array positions and the logarithmic fitting function.

Acknowledgements
The figures were generated using Generic Mapping Tools software (Wessel and Smith 1998). In addition, we thank Editage (www.editage.jp) for English language editing.

Authors' contributions
FT carried out all data analysis and wrote the manuscript. MK provided basic concept of the approximate travel-time calculation, contributed to discussion and interpretation, and improved the developed technique and the manuscript. All authors read and approved the final manuscript.

Funding
This study was supported by Japan Society for the Promotion of Science (JSPS) KAKENHI (Grant No. 20K14588).

Availability of data and materials
The GNSS-acoustic observational data collected by the Japan Coast Guard at KAMN, KAMS, MYGI, MYGW, FUKU, and CHOS have been distributed in Zenodo, as shown by Watanabe et al. (2021). Array displacements at KAMN, KAMS, MYGI, MYGW, FUKU, and CHOS were distributed on the homepage of the Japan Coast Guard by Yokota et al. (2018b). The GNSS-acoustic observational data collected by Tohoku University for G10, G17, and G20 are available from the authors upon request. The GNSS-A positioning programs (Methods 1–3 in "Application of the MCMC-based array positioning method" section; they are written in Julia) are available from the authors upon request.

Declarations

Ethics approval and consent to participate
No applicable.

Consent for publication
No applicable.

Competing interests
The author declares that they have no competing interests.

Received: 19 July 2022 Accepted: 9 November 2022
Published online: 02 December 2022

References

Akaike H (1980) Likelihood and the Bayes procedure. In: Bernardo JM, DeGroot MH, Lindley DV, Smith AFM (eds) Bayesian statistics. University Press, London, pp 143–166

Bayes T (1763) An essay towards solving a problem in the doctrine of chances. Phil Trans R Soc 53:370–418. https://doi.org/10.1098/rstl.1763.0053

Chadwell CD, Sweeney AD (2010) Acoustic ray-trace equations for seafloor geodesy. Mar Geod 33:164–186. https://doi.org/10.1080/01490419.2010.492283

Fujita M, Ishikawa T, Mochizuki M, Sato M, Toyama S, Katayama M (2006) GPS/acoustic seafloor geodetic observation: method of data analysis and its application. Earth Planets Space 58:265–275. https://doi.org/10.1186/BF03351923

Fujiwara S, Tobita M, Ozawa S (2022) Spatiotemporal functional modeling of postseismic deformations after the 2011 Tohoku-Oki earthquake. Earth Planets Space 74:13. https://doi.org/10.1186/s40623-021-01568-0

Fukuda J, Johnson KM (2008) A fully Bayesian inversion for spatial distribution of fault slip with objective smoothing. Bull Seis Soc Am 98(3):1128–1146. https://doi.org/10.1785/0120070194

Hastings WK (1970) Monte Carlo sampling methods using Markov chains and their applications. Biometrika 57:97–109. https://doi.org/10.1093/biomet/57.1.97

Honsho C, Kido M (2017) Comprehensive analysis of traveltime data collected through GPS-acoustic observation of seafloor crustal movements. J Geophys Res 122:8583–8599. https://doi.org/10.1002/2017JB014733

Honsho C, Kido M, Tomita F, Uchida N (2019) Offshore postseismic deformation of the 2011 Tohoku earthquake revisited: application of an improved GPS-acoustic positioning method considering horizontal gradient of sound speed structure. J Geophys Res 124:5990–6009. https://doi.org/10.1029/2018JB017135

Honsho C, Kido M, Ichikawa T, Ohashi T, Kawakami T, Fujimoto H (2021) Application of phase-only correlation to travel-time determination in GNSS-acoustic positioning. Front Earth Sci 9:600732. https://doi.org/10.3389/feart.2021.600732

Iinuma T, Hino R, Kido M, Inazu D, Osada Y, Ito Y, Ohzono M, Tsushima H, Suzuki S, Fujimoto H, Miura S (2012) Coseismic slip distribution of the 2011 off the Pacific Coast of Tohoku Earthquake (M9.0) refined by means of seafloor geodetic data. J Geophys Res 117:B07409. https://doi.org/10.1029/2012JB009186

Ikuta R, Tadokoro K, Ando M, Okuda T, Sugimoto S, Takatami K, Yada K, Besana GM (2008) A new GPS-acoustic method for measuring ocean floor crustal deformation: application to the Nankai Trough. J Geophys Res 113:B02401. https://doi.org/10.1029/2006JB004875

Kido M (2007) Detecting horizontal gradient of sound speed in ocean. Earth Planets Space 59:33–36. https://doi.org/10.1186/BF03352027

Kido M, Fujimoto H, Miura S, Osada Y, Tsuka K, Tabei T (2006) Seafloor displacement at Kumano-nada caused by the 2004 off Kii Peninsula earthquakes, detected through repeated GPS/Acoustic surveys. Earth Planets Space 58:911–915. https://doi.org/10.1186/BF03351996

Kido M, Osada Y, Fujimoto H, Hino R, Ito Y (2011) Trench-normal variation in observed seafloor displacements associated with the 2011 Tohoku-Oki earthquake. Geophys Res Lett 38:L24303. https://doi.org/10.1029/2011GL050057

Kinugasa N, Tadokoro K, Kato T, Terada Y (2020) Estimation of temporal and spatial variation of sound speed in ocean from GNSS-A measurements for observation using moored buoy. Prog Earth Planet Sci 7:21. https://doi.org/10.1186/s40645-020-00331-5

Kubo H, Asano K, Iwata T, Aoi S (2016) Development of fully Bayesian multiple-time-window source inversion. Geophys J Int 204(3):1601–1619. https://doi.org/10.1093/gji/ggv540

Locarnini RA, Mishonov AV, Baranova OK, Boyer TP, Zweng MM, Garcia HE, Reagan JR, Seidov D, Weathers K, Paver CR, Smolyar I (2018) World Ocean Atlas 2018, volume 1: temperature. A. Mishonov Technical Ed., NOAA Atlas NESDIS, vol 81, p 52

Matsui R, Kido M, Niwa Y, Honsho C (2019) Effects of disturbance of seawater excited by internal wave on GNSS-acoustic positioning. Marine Geophys Res 40:541–555. https://doi.org/10.1007/s11001-019-09394-6

Metropolis N, Rosenbluth AW, Rosenbluth MN, Teller AH, Teller E (1953) Equation of state calculations by fast computing machines. J Chem Phys 21:1087–1092. https://doi.org/10.1063/1.1699114

Sato M, Ishikawa T, Ujihara N, Yoshida S, Fujita M, Mochizuki M, Asada A (2011) Displacement above the hypocenter of the 2011 Tohoku-Oki earthquake. Science 332(6036):1395. https://doi.org/10.1126/science.1207401

Schwartz G (1978) Estimating the dimension of a model. Ann Statist 6(2):461–464. https://doi.org/10.1214/aos/1176344136

Spiess FN (1985) Suboceanic geodetic measurements. IEEE Trans Geosci Rem Sens GE-23(4):502–510. https://doi.org/10.1109/TGRS.1985.289441

Spiess FN, Chadwell CD, Hildebrand JA, Young LE, Purcell GH Jr, Dragert H (1998) Precise GPS/acoustic positioning of seafloor reference points for tectonic studies. Phys Earth Planet Int 108(2):101–112. https://doi.org/10.1016/S0031-9201(98)00089-2

Tomita F, Kido M, Osada Y, Hino R, Ohta Y, Iinuma T (2015) First measurement of the displacement rate of the Pacific Plate near the Japan Trench after the 2011 Tohoku-Oki earthquake using GPS/acoustic technique. Geophys Res Lett 42:8391–8397. https://doi.org/10.1002/2015GL065746

Tomita F, Kido M, Ohta Y, Iinuma T, Hino R (2017) Along-trench variation in seafloor displacements after the 2011 Tohoku earthquake. Sci Adv 3(7):e1700113. https://doi.org/10.1126/sciadv.1700113

Tomita F, Kido M, Honsho C, Matsui R (2019) Development of a kinematic GNSS-acoustic positioning method based on a state-space model. Earth Planets Space 71:102. https://doi.org/10.1186/s40623-019-1082-y

Tomita F, Iinuma T, Agata R, Hori T (2021) Development of a trans-dimensional fault slip inversion for geodetic data. J Geophys Res 126:e2020JB020991. https://doi.org/10.1029/2020jb020991

Watanabe S, Ishikawa T, Yokota Y, Nakamura Y (2020) GARPOS: analysis software for the GNSS-A seafloor positioning with simultaneous estimation of sound speed structure. Front Earth Sci 8:597532. https://doi.org/10.3389/feart.2020.597532

Watanabe S, Ishikawa T, Nakamura Y, Yokota Y (2021) Co- and postseismic slip behaviors extracted from decadal seafloor geodesy after the 2011 Tohoku-oki earthquake. Earth Planets Space 73:162. https://doi.org/10.1186/s40623-021-01487-0
Wessel P, Smith WHF (1998) New, improved version of generic mapping tools released. Eos Trans AGU 79(47):579. https://doi.org/10.1029/98eo00426
Yabuki T, Matsu'ura M (1992) Geodetic data inversion using a Bayesian information criterion for spatial distribution of fault slip. Geophys J Int 109(2):363–375. https://doi.org/10.1111/j.1365-246X.1992.tb00102.x
Yasuda K, Tadokoro K, Taniguchi S, Kimura H, Matsuhiro K (2017) Interplate locking condition derived from seafloor geodetic observation in the shallowest subduction segment at the Central Nankai Trough, Japan. Geophys Res Lett 44:3572–3579. https://doi.org/10.1002/2017GL072918
Yokota Y, Ishikawa T (2020) Shallow slow slip events along the Nankai Trough detected by GNSS-A. Sci Adv 6(3):eaay5786. https://doi.org/10.1126/sciadv.aay5786
Yokota Y, Ishikawa T, Watanabe S, Tashiro T, Asada A (2016) Seafloor geodetic constraints on interplate coupling of the Nankai Trough megathrust zone. Nature 534:374–377. https://doi.org/10.1038/nature17632
Yokota Y, Ishikawa T, Watanabe S (2018a) Gradient field of undersea sound speed structure extracted from the GNSS-A oceanography. Mar Geophys Res 40:493–504. https://doi.org/10.1007/s11001-018-9362-7
Yokota Y, Ishikawa T, Watanabe S (2018b) Seafloor crustal deformation data along the subduction zones around Japan obtained by GNSS-A observations. Sci Data 5:180182. https://doi.org/10.1038/sdata.2018.182
Zweng MM, Reagan JR, Seidov D, Boyer TP, Locarnini RA, Garcia HE, Mishonov AV, Baranova OK, Weathers K, Paver CR, Smolyar I (2018) World Ocean Atlas 2018, volume 2: salinity. A. Mishonov Technical Ed., NOAA Atlas NESDIS, vol 82, p 50

Publisher's Note